The mantle transition zone as seen by global *Pds* phases: No clear evidence for a thin transition zone beneath hotspots

Benoit Tauzin,[1] Eric Debayle,[1] and Gérard Wittlinger[1]

[1]   We present a new global study of the transition zone from *Pds* converted waves at the 410- and 660-km discontinuities. Our observations extend previous global *Pds* studies with a larger data set, especially in oceanic regions where we have been able to measure *Pds* travel times, sampling the mantle transition zone (MTZ) beneath 26 hotspot locations. We find significant lateral variations of the MTZ thickness. Both the maximum variations ($\pm35-40$ km) and the long-wavelength pattern are in overall agreement with previous SS precursors studies. The MTZ is generally thick beneath subduction zones, where the observed MTZ variations are consistent with thermal anomalies ranging between $-100°$K and $-300°$K. In Central and North America, we observe an NW$-$SE pattern of thick MTZ, which can be associated with the fossil Farallon subduction. We do not find clear evidence for a thin MTZ beneath hotspots. However, the 410-km discontinuity remains generally deepened after correcting our *Pds* travel times for the 3D heterogeneities located above the MTZ, and its topography variations can be explained by thermal anomalies between $+100°$K and $+300°$K. The depth of the 660-km discontinuity may be less temperature sensitive in hot regions of the mantle, which is consistent with the effect of a phase transition from majorite garnet to perovskite at a depth of 660 km.

1.   Introduction

[2]   Most recent studies of the mantle transition zone (MTZ) 410-km and 660-km seismic discontinuities have been based on reflected and converted waves [e.g., *Shearer*, 1991; *Flanagan and Shearer*, 1998; *Gu et al.*, 1998; *Chevrot et al.*, 1999; *Deuss et al.*, 2006; *Lawrence and Shearer*, 2006].

[3]   Underside reflections as precursors of SS waves sample the MTZ discontinuities near the bounce point, half way between source and receiver. They provide a good global coverage of the MTZ, but they are generally analyzed at periods greater than 25 s, which limits their lateral resolution to a few thousands kilometers, due to their large X-shaped Fresnel zones near the bounce point. SS precursor results suggest significant amplitudes of MTZ thickness variations (±40 km), with a positive correlation between thick MTZ and subduction zones. The MTZ is also generally found to be thinner beneath oceanic regions than beneath continents [*Gu and Dziewonski*, 2002; *Li et al.*, 2003]. *Deuss* [2007] analyzed SS precursors beneath 26 hotspots in the period range $15-75$ s. She observed a thin MTZ beneath two thirds of the hotspots. The other hotspots are characterized by a clear deepening of the 410-km and 660-km discontinuities, which can be explained by the uppermost

mantle velocity structure or the effect of the majorite garnet to perovskite phase transition. This phase transition could be dominant in regions with high mantle temperatures, where it occurs near 660-km depth, with a positive Clapeyron slope, opposite to the postspinel phase boundary [*Hirose*, 2002]. It is however likely that long-period SS precursors do not provide sufficient lateral resolution to detect narrow thermal plumes. The majorite garnet to perovskite phase transition hypothesis needs therefore to be tested with a data set providing a better lateral resolution. This is one of the aims of the present study.

[4]   P-to-S converted waves at a seismic discontinuity *d* (hereafter referred as *Pds*) provide a better lateral resolution beneath the stations. The first Fresnel zone at 10 s period can be approximated by a circular horizontal section with a radius of $150-200$ kilometers at MTZ depths [*Wittlinger and Farra*, 2007]. *Pds* waves are however less suited to global studies, owing to the limited geographic distribution of seismometers, especially in oceanic areas. Recently, *Chevrot et al.* [1999] (hereafter referred to as CVM99) measured and compiled 82 *Pds* travel times at stations mostly located inland, away from hotspots and subduction zones. They found weak variations of the MTZ thickness (±10 km). In addition, their pattern of MTZ variations showed no significant correlations with results of SS precursors studies. *Lawrence and Shearer* [2006] (hereafter referred to as LS06) measured *Pds* travel times beneath 118 global seismic stations, with a better coverage of subduction

---

[1]Ecole et Observatoire des Sciences de la Terre, CNRS and ULP, Strasbourg, France.
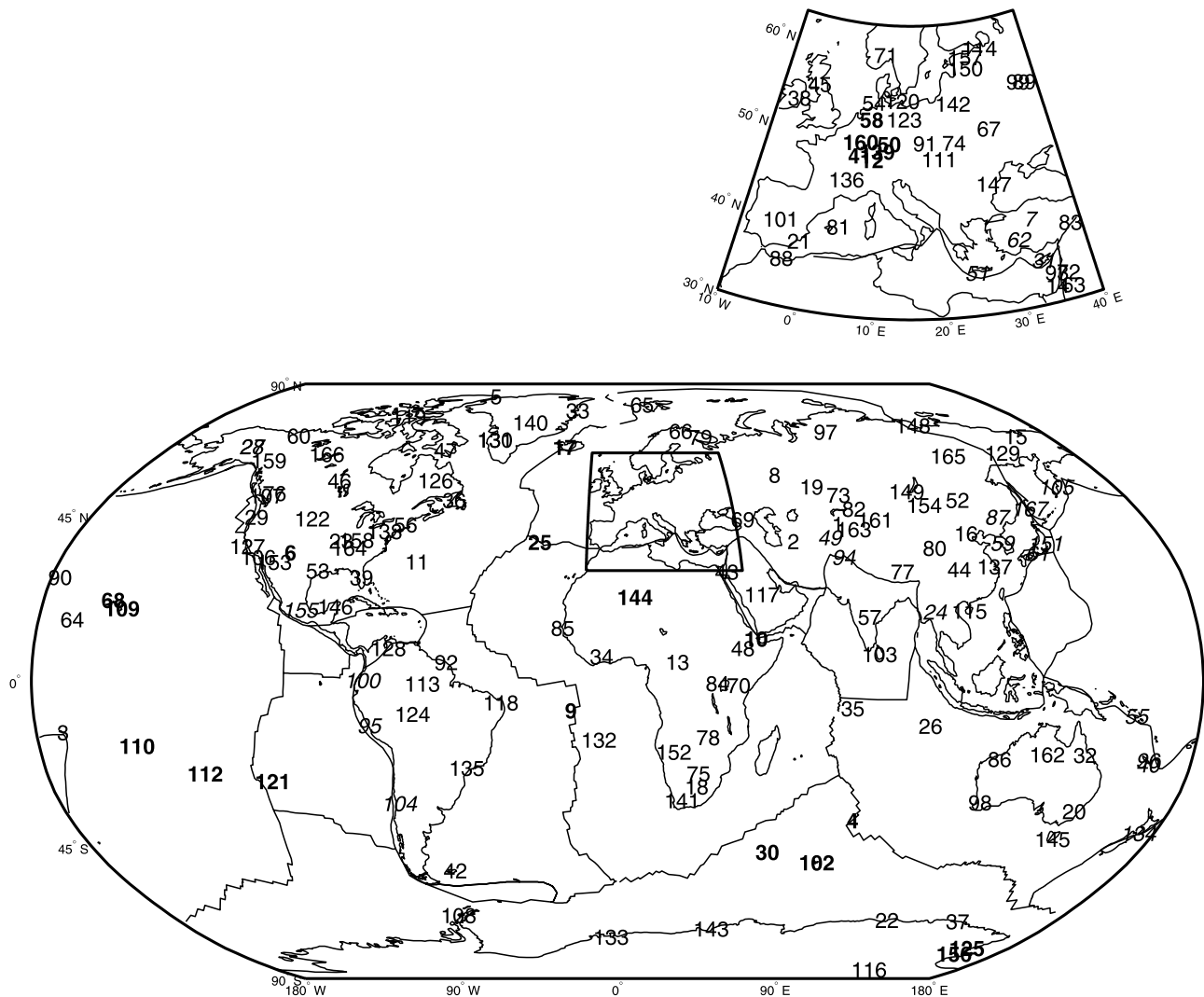
Figure 1. Map showing the location of 167 FDSN stations for which we have been able to measure *Pds* travel times. Each station is labeled with a number referring to the first column in Table 1, where more detailed information is provided. Weight and angles of fonts refer to the tectonic provinces to which the stations are assumed to belong (bold for "plumes", italic for "subductions", and normal for "normal mantle").

zones and oceanic regions. In contrast to CVM99, their globally averaged MTZ thickness, amplitude and long-wavelength pattern of MTZ thickness variations show good agreement with SS precursor results. They attributed the observed differences with CVM99 to their improved coverage of subductions and oceanic regions and the bias introduced by the use of a constant ray parameter approximation in CVM99.

[5] At regional scale, several *Pds* studies [*Thirot et al.*, 1998; *Gilbert et al.*, 2001; *Li and Yuan*, 2003; *Liu et al.*, 2003; *van der Meijde et al.*, 2005] suggest significant thickening of the MTZ beneath subduction zones. *Li et al.* [2003] (hereafter referred as L03) studied *Pds* waves beneath 18 seismic stations located on oceanic islands near hotspots locations, and found MTZ thicknesses similar, or up to 15% thinner than in IASP91.

[6] Our present study extends recent global works by CVM99 and LS06 with a larger data set. We have measured

Pds arrivals converted at the 410-km and 660-km discontinuities beneath a total of 167 stations (Figure 1). These observations are currently the largest available data base of mantle *Pds* phases measured in a consistent way. They provide an improved coverage of the MTZ near hotspots, and to a lesser extent subduction zones. This allows us to compare the MTZ structure beneath stations belonging to different tectonics environments.

2. Data Processing

[7] *Pds* arrivals result from teleseismic P waves that convert a portion of their energy into shear waves at an interface located at depth *d* (Figure 2). The amplitude of *Pds* phases does not exceed few percent of the direct P wave. To measure such weak secondary phases, it is necessary to stack large number of seismograms corresponding to different events recorded at the same station [*Vinnik*, 1977].
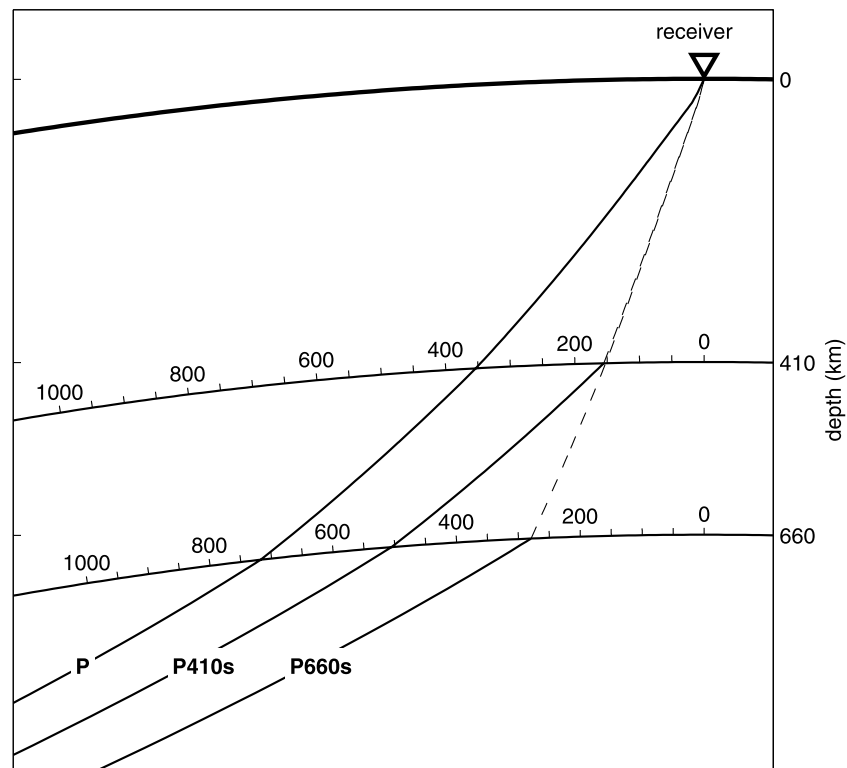
Figure 2. *Pds* ray paths after ray tracing in the IASP91 velocity model [*Kennett and Engdahl*, 1991] for an event located at a distance of 40° from the station. Solid lines indicate *P* waves. Dashed lines indicate S-waves. The distance in kilometers from the receiver is indicated along the 410-km and 660-km discontinuities. For an epicentral distance of 40° the conversion points at the 410-km and 660-km discontinuities are shifted laterally from the station by 150 km and 250 km.

Differences between effective source time functions associated with each event can cause significant differences in the waveforms so we equalize the data through the building of a receiver function [*Langston*, 1979].

2.1. Building the Receiver Functions

[8] We build receiver functions from the deconvolution of the record rotated along the P-axis from the record rotated along the SV-axis. The P-SV-SH configuration is better than a standard Vertical-Radial-Transverse configuration as energy of weak secondary *Pds* arrivals is enhanced on both SV and SH components.

[9] The P-axis record is used as an approximation of the source time function convolved with the instrument. We use the iterative deconvolution method described by *Ligorria and Ammon* [1999] to obtain a time series showing the response of the Earth structure beneath the receiver.

2.2. Data Selection

[10] We selected earthquakes with magnitudes higher than 6.0 recorded between 1986 and 2006. The data are 3-component seismograms corresponding to epicentral distances ranging from 40° to 95° and recorded at broad-band stations (Figure 1) from eight global and regional permanent arrays.

[11] To allow comparison of seismograms recorded with different instruments, all the data are deconvolved from their original instrument and then reconvolved with the transfer function of the Geoscope station PAF. The records

are afterward band-pass filtered using a Butterworth filter in the period range 10–25 s. Several criteria are then applied to select the best quality data. After rotating each component, we compute the ratio between the maximum amplitude of the signal (measured on the P-axis, in a time window starting 5 s before and ending 25 s after the P theoretical arrival) and the averaged root-mean-square of the SV and SH components. All seismograms for which this signal to noise ratio is lower than 5 are discarded. After iterative deconvolution, we reject receiver functions showing significant signal before the *P* wave spike or large amplitudes (greater than 20% of the *P* wave spike) in the time window 25–90 s after the *P* wave arrival. At this stage, we also discard receiver functions for which the converted phase is not present for both the 410- or 660-km discontinuities. This is done through an automated search for significant positive amplitudes in a time window spanning ±7 s around the *P*410*s* and *P*660*s* theoretical arrivals.

[12] Figure 3 diplays two receiver function sections, obtained after applying our selection criteria on the waveforms recorded at two stations TAM and PPT. In general, oceanic stations such as PPT show a greater noise level compared with continental stations such as TAM.

2.3. Stacking Approach

[13] The amplitude of *Pds* phases converting at MTZ discontinuities is generally smaller than 4% of the *P* wave amplitude. A stacking approach is therefore used to increase the signal to noise ratio. The stacking procedure includes
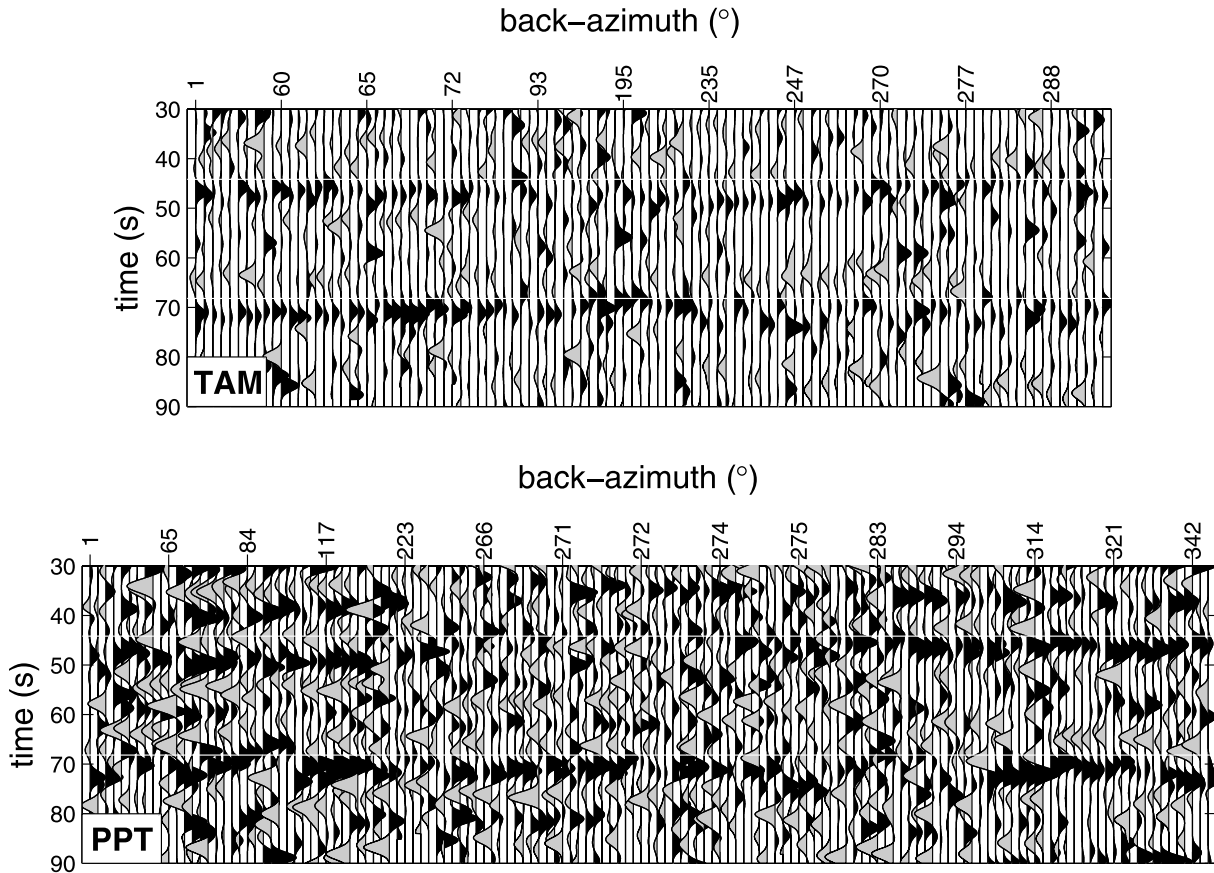
Figure 3. Receiver function sections for the continental station TAM in Africa (quality 1) and the oceanic station PPT in the South Pacific Ocean (quality 2). Original seismograms were filtered in the $10-25$ s period range. Each section is obtained by assembling all the receiver functions selected for the stack and sorted by back azimuths. Receiver functions are move-out corrected for a reference epicentral distance of $65°$. Horizontal thin white lines show the $P410s$ and $P660s$ arrival times in IASP91.

corrections for the differences in travel times due to different incidence angles at the station. For each station, we build a slant stack of the selected receiver functions. We first align receiver functions on the P wave arrival times. We apply linear move-out corrections on Pds hodochrons (t_{Pds}) using the relation:

$$\tau = t_{Pds} - \delta p \cdot (\Delta - \Delta_r).$$

[14] τ is the corrected travel time of the Pds-wave at the reference distance $\Delta_r = 65°$ and δp is the differential slowness of converted waves relative to P at distance Δ. We test a range of δp values from -0.35 to 0.35 s/$°$ relative to the slowness of the direct P arrival. For each value of δp, the entire series in the (t, Δ) domain is converted to a single trace that is a function of τ. The slant stack is the resulting alignment of traces in the ($\tau, \delta p$) domain. Figure 4 displays slant stacks for data at TAM and PPT stations. From a theoretical ($\tau, \delta p$) curve computed in the IASP91 [*Kennett and Engdahl*, 1991] 1-D velocity model at $65°$ reference distance (black thick curves in Figure 4), we extract the final stacked move-out corrected receiver functions. Our approach therefore uses the theoretical IASP91 ray parameter of the Pds phases, and does not rely on the constant

ray parameter approximation used in many prior Pds studies. The absolute travel times $t_{Pds}-t_P$ are then measured on the resulting stacked receiver functions (Figure 5).

2.4. Quality Criterion

[15] Our stacked receiver functions (Figure 5) are classified in four groups, depending on a quality criterion. This criterion allows us to attribute a confidence level to the travel-time measurements made at each station. It takes into account the noise level and the consistency of waveforms on the receiver function sections, the level of focusing of stacked $P410s$ and $P660s$ energy in the ($\tau, \delta p$) diagrams and the signal to noise ratio on the stacked receiver functions.

[16] The quality 1 stations present the highest signal to noise ratio at each step of the processing. The quality 2 stations show a lower signal to noise ratios on the initial receiver function section and on the ($\tau, \delta p$) diagram but their stacks still provide high-quality waveforms. Examples of typical receiver function sections and slant-stack diagrams for quality 1 and 2 stations are shown on Figures 3 and 4. Quality 3 and 4 stacked receiver functions are noisy and often correspond to stations where a small number of data could be stacked.
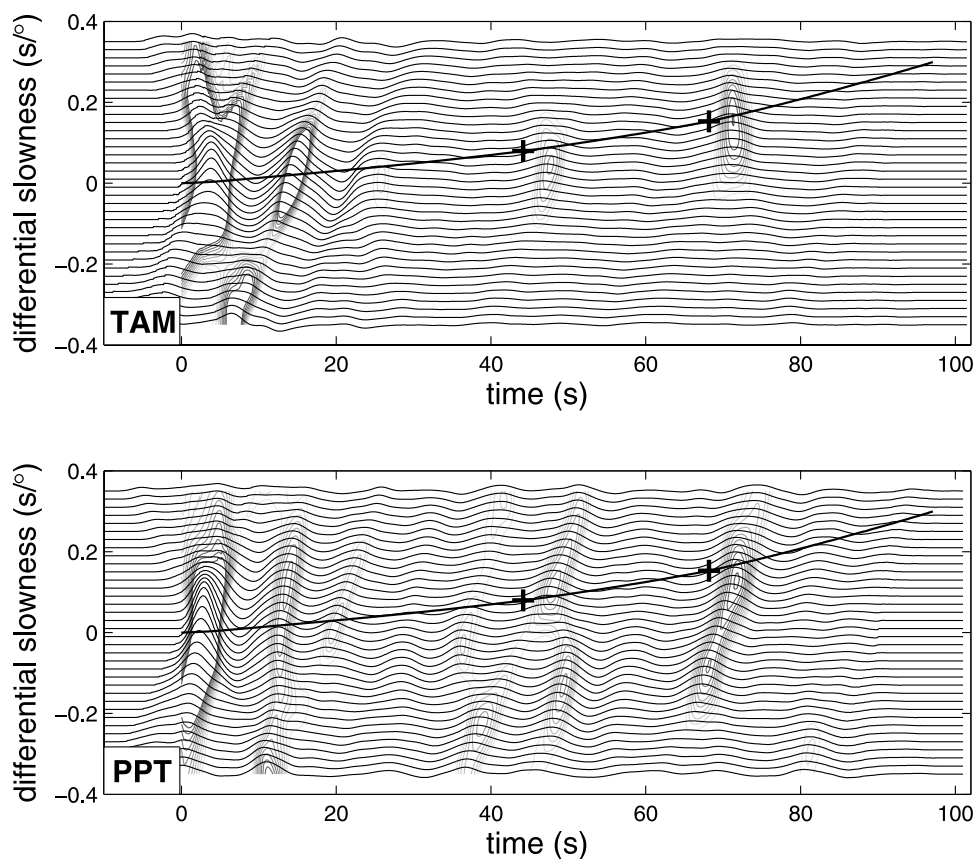
Figure 4. Example of slant-stack diagrams obtained at TAM (quality 1) and PPT (quality 2) stations. The corresponding seismic sections are shown in Figure 3. Travel times τ for a reference distance of 65° are plotted on the x-axis. The differential slownesses p are shown on the y-axis. The black curves are (τ, p) couples predicted by IASP91 [*Kennett and Engdahl*, 1991]. The theoretical time-slowness pairs for the $P410s$ and $P660s$ arrivals are shown with the black crosses.

[17] From an initial number of 221 stations, we discuss our results for the 167 quality 1 and 2 stations shown in Figure 1 and listed in Table 1.

3. Results

[18] The reference model for the interpretation of our travel times is the IASP91 velocity model [*Kennett and Engdahl*, 1991]. In this model, the MTZ is 250 km thick and bounded by two discontinuities, located at 410- and 660-km depths. Ray tracing with a surface event and recorded at an epicentral distance of 65° predicts Pds conversions at the 410- and 660-km discontinuities arriving 44.2 s and 68.2 s after the direct P arrival. This corresponds to a reference differential travel time of 24 s. Although changing the depth of the source produces different incidence angles at the 410- and 660-km discontinuities, we checked that this effect can be neglected in our period range of analysis (>10 s), as it is averaged out in the stacking procedure.

[19] We use the RUM model by *Gudmundsson and Sambridge* [1998] and a compilation of 65 hotspot locations by *Anderson and Schramm* [2005] to sort our stations (Figure 6). We obtain 24 quality 1 or 2 stations located near active subduction zones (subduction stations). Pds waves recorded at these stations are likely to have sampled

a cold subducted slab within the MTZ. A total of 22 stations are located near 15 of the 65 hotspots of the *Anderson and Schramm* [2005] list. Pds waves recorded at these stations may have sampled a hot thermal plume, if present beneath the hotspot. One station (AFI) belongs to both subduction and hotspot group of stations. Pds waves recorded at the 122 remaining stations are assumed to have sampled a "normal MTZ" region, corresponding to the part of the MTZ which does not belong to the two other provinces. The stations and their corresponding "tectonic provinces" are listed in Table 2.

3.1. Absolute Travel Times

[20] Absolute t_{Pds} travel times and apparent depths of the discontinuities show large variations around the reference values from IASP91 (Figures 7a and 7b). Observed $P410s$ travel times range between −4 s to +5.7 s around the IASP91 reference value with extrema at stations Urumqi (WMQ) in China and Palmer Station (PMSA) in Antarctica (Table 1). $P660s$ arrival times range from −3 s to +5.8 s around IASP91, with extrema values at Gavdos Island (GVD) in the Aegean subduction zone and Mount Furi (FURI) in Ethiopia (Table 1). Standard deviations in both distributions (1.9 and 1.7 s) are five to six times larger than the typical station standard error.
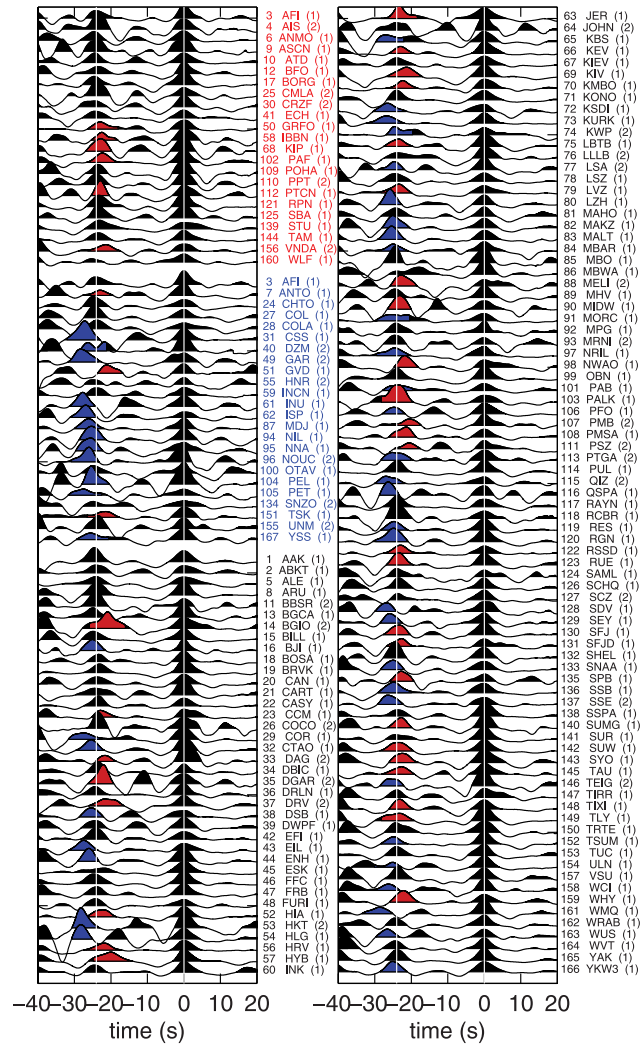
Figure 5. The 167 final receiver functions used to measure our differential and absolute travel times. The waveforms are aligned on the observed $P_{660}s$ arrival times. The $P_{660}s$ and $P_{410}s$ arrival times in IASP91 are indicated with the vertical white lines. Receiver functions with differential travel-time anomalies greater than 1 s with respect to the 24 s reference time of IASP91 have their $P_{410}s$ waveforms colored in red (<23 s) or blue (>25 s). Red, blue and black colors are used for numbers and names of stations belonging to the "hotspot", "subduction", or "normal mantle" MTZ provinces, respectively. Numbers in parentheses are the quality criteria associated to each stack. See Figure 1 for station locations and Table 1 for the details of our travel-time measurements.

[21] It is well known that t_{Pds} travel times are sensitive to the strong 3-D velocity heterogeneities in the top of the upper mantle [e.g., *Chevrot et al.*, 1999]. Figure 8 displays a comparison between our t_{P410s} residuals (defined as t_{P410s} observed minus t_{P410s} predicted by IASP91) and a vertical average of seismic heterogeneities in the top 410 km of the DKP2005 shear-wave tomographic model [*Debayle et al.*, 2005]. There is a good overall agreement between our $tP410s$ residuals and the distribution of vertical averaged shear wave velocities above the MTZ (Figure 8). Slow

seismic velocities observed beneath oceanic areas, mid-oceanic ridges or the Paleozoic lithosphere of continents are generally associated with positive t_{P410s} residuals while high seismic velocities beneath cratons correlate well with negative t_{P410s} residuals. The most significant disagreements are observed at HYB (47.9 ± 0.2 s) in India and NWAO (45.2 ± 0.2 s) in Australia. Figure 8 confirms that shallow seismic heterogeneities are an important source of variation in $P410s$ travel times.

3.2. Differential Travel Times and the Apparent MTZ Thickness

[22] Differential travel times $t_{P660s} - t_{P410s}$ are sensitive to variations in discontinuity depths and velocity heterogeneities within the MTZ. If the depth location of seismic discontinuities is controlled by phase changes from olivine α to β phases and γ-spinel to perovskite + magnesiowüstite at pressure equivalent to 410-km and 660-km depths, cold (hot) temperature anomalies will cause thickening (thinning) of the transition zone because of the opposite clapeyron slopes of the 410- and 660-km phase transitions.

[23] The distribution of differential travel times (apparent MTZ thickness in IASP91) for our global data set has an average of 24.2 s (253 km) and a standard deviation of 1.6 s (16 km, Figure 9a). Extrema values are observed in the Eurasian continent at stations WMQ (28.8 ± 0.4 s or 295 ± 4 km) and HYB (20 ± 0.2 s or 208 ± 2 km). For the normal MTZ subset of stations, the distribution of differential travel times is similar to the one observed for the entire data set, with equivalent averages and standard deviations (Figure 9b). However, hotspot and subduction stations have respectively smaller and larger average values: 23.5 s (247 km) and 25.2 s (263 km) with 0.8 (8 km) and 1.9 s (19 km) standard deviation (Figures 9c and 9d).

[24] Figure 10 shows our differential travel times superimposed to the distribution of hotspots and subductions. Figures 5 and 10 show that stations belonging to the subduction province are generally associated with a thick MTZ. Half of the 24 subduction stations (PET, YSS, MDJ, INU, NNA, and PEL in South America, ISP and CSS near the Aegean subduction zone, GAR and NIL near the Hindu subduction and NOUC and DZM in New Hebrides) show differential travel times larger than 25 s. Three stations (CHTO, OTAV and SNZO) add to this list if we consider differential travel times greater than 24.5 s. Only three stations (ANTO, GVD and TSK) show up with travel times smaller than 23 s. Figures 5 and 10 show that a thin MTZ is generally not clearly observed beneath stations located within the "hotspot" province. Among the 22 stations belonging to the "hotspot" province, 16 are within 1 s of the 24 s reference travel time predicted by IASP91. Six stations (GRFO, IBBN, KIP, PAF, PTCN, VNDA) support more clearly a thin transition zone, with travel times smaller than 23 s. A proportion of 58% of the normal MTZ subset of stations have differential travel times within ±1 s of the 24 s predicted by IASP91.

3.3. Travel Time Corrections and Corrected Depth of the 410-km Discontinuity

[25] Deviations from IASP91 (Figures 7a and 7b) can be partly explained by effects of 3D velocity perturbations relative to IASP91 above the MTZ (Figure 8). We have used

Table 1. Travel-Time Measurements at Our 167 Quality 1 and 2 Stations

	Station	Lat, °	Lon, °	Number	Quality	t_{P410s}, s	t_{P660s}, s	Δt, s	Context
1	AAK	42.64	74.49	451	1	44.9 ± 0.1	69.4 ± 0.2	24.6 ± 0.2	normal mantle
2	ABKT	37.93	58.12	181	1	44.2 ± 0.5	68.5 ± 0.5	24.2 ± 0.7	normal mantle
3	AFI	−13.91	−171.78	160	1	46.3 ± 0.7	70.5 ± 0.2	24.1 ± 0.7	hotspot and subduction
4	AIS	−37.80	77.57	43	2	46.4 ± 0.4	69.8 ± 0.8	23.3 ± 0.8	hotspot
5	ALE	82.50	−62.35	337	1	44.5 ± 0.2	68.5 ± 0.4	24.1 ± 0.5	normal mantle
6	ANMO	34.95	−106.46	396	1	46.7 ± 0.1	71.2 ± 0.2	24.6 ± 0.2	hotspot
7	ANTO	39.87	32.79	152	1	47.4 ± 0.3	70.3 ± 0.2	22.9 ± 0.4	subduction
8	ARU	56.43	58.56	324	1	43.5 ± 0.3	67.4 ± 0.1	23.9 ± 0.3	normal mantle
9	ASCN	−7.93	−14.36	68	1	47.2 ± 1.1	70.6 ± 0.6	23.4 ± 1.2	hotspot
10	ATD	11.53	42.85	98	1	48.2 ± 0.2	72.6 ± 0.4	24.4 ± 0.5	hotspot
11	BBSR	32.37	−64.70	68	2	46.3 ± 0.2	70.4 ± 0.3	24.1 ± 0.3	normal mantle
12	BFO	48.33	8.33	140	1	44.5 ± 0.5	68.2 ± 0.1	23.7 ± 0.5	hotspot
13	BGCA	5.18	18.42	68	1	41.6 ± 0.3	66.5 ± 0.3	24.9 ± 0.4	normal mantle
14	BGIO	31.72	35.09	60	2	45.7 ± 0.2	66.7 ± 0.4	21.0 ± 0.4	normal mantle
15	BILL	68.07	166.45	253	1	44.0 ± 0.2	68.9 ± 0.1	24.9 ± 0.2	normal mantle
16	BJI	40.04	116.18	40	1	45.9 ± 0.3	71.0 ± 0.1	25.0 ± 0.4	normal mantle
17	BORG	64.75	−21.33	172	1	48.5 ± 0.3	73.0 ± 0.1	24.5 ± 0.3	hotspot
18	BOSA	−28.61	25.26	116	1	42.2 ± 0.2	65.5 ± 0.2	23.3 ± 0.3	normal mantle
19	BRVK	53.06	70.28	334	1	44.0 ± 0.1	67.1 ± 0.2	23.1 ± 0.2	normal mantle
20	CAN	−35.32	149.00	198	1	45.8 ± 0.5	69.5 ± 0.3	23.7 ± 0.6	normal mantle
21	CART	37.59	−1.00	127	1	45.1 ± 0.8	69.5 ± 0.2	24.5 ± 0.8	normal mantle
22	CASY	−66.28	110.54	221	1	44.9 ± 0.1	68.2 ± 0.4	23.3 ± 0.4	normal mantle
23	CCM	38.06	−91.24	157	1	43.9 ± 0.3	66.8 ± 0.7	22.9 ± 0.7	normal mantle
24	CHTO	18.79	98.98	344	1	44.1 ± 0.2	69.0 ± 0.4	24.9 ± 0.5	subduction
25	CMLA	37.76	−25.52	88	2	47.2 ± 0.2	71.2 ± 0.7	24.0 ± 0.8	hotspot
26	COCO	−12.19	96.83	32	2	44.9 ± 0.4	68.4 ± 1.5	23.5 ± 1.5	normal mantle
27	COL	64.90	−147.79	155	1	42.4 ± 0.2	66.9 ± 0.3	24.5 ± 0.3	subduction
28	COLA	64.87	−147.85	464	1	42.7 ± 0.2	66.5 ± 0.3	23.8 ± 0.3	subduction
29	COR	44.59	−123.30	246	1	43.2 ± 1.4	70.7 ± 0.3	27.5 ± 1.5	normal mantle
30	CRZF	−46.43	51.86	94	2	46.4 ± 1.3	70.8 ± 0.2	24.4 ± 1.4	hotspot
31	CSS	34.96	33.33	121	1	42.8 ± 0.2	69.9 ± 0.3	27.2 ± 0.3	subduction
32	CTAO	−20.09	146.25	200	1	44.7 ± 0.2	70.1 ± 0.1	25.4 ± 0.3	normal mantle
33	DAG	76.77	−18.66	71	2	44.2 ± 0.6	65.9 ± 1.2	21.7 ± 1.3	normal mantle
34	DBIC	6.67	−4.86	94	1	42.0 ± 0.1	65.5 ± 0.1	23.5 ± 0.2	normal mantle
35	DGAR	−7.41	72.45	39	2	44.5 ± 0.2	66.7 ± 1.0	22.2 ± 1.0	normal mantle
36	DRLN	49.26	−57.50	138	1	43.3 ± 0.2	67.5 ± 0.2	24.2 ± 0.3	normal mantle
37	DRV	−66.67	140.00	222	2	45.6 ± 1.0	67.2 ± 0.1	21.6 ± 1.0	normal mantle
38	DSB	53.25	−6.38	145	1	43.8 ± 0.3	69.2 ± 0.8	25.4 ± 0.9	normal mantle
39	DWPF	28.11	−81.43	56	1	45.3 ± 0.9	69.4 ± 0.3	24.1 ± 1.0	normal mantle
40	DZM	−22.07	166.44	23	2	45.8 ± 1.5	71.9 ± 0.5	26.2 ± 1.6	subduction
41	ECH	48.22	7.16	222	1	44.0 ± 0.3	68.4 ± 0.2	24.4 ± 0.4	hotspot
42	EFI	−51.68	−58.06	97	1	44.3 ± 0.4	68.5 ± 0.5	24.2 ± 0.6	normal mantle
43	EIL	29.67	34.95	134	1	43.5 ± 0.3	70.9 ± 0.4	27.5 ± 0.5	normal mantle
44	ENH	30.27	109.49	80	1	43.2 ± 0.3	69.2 ± 0.5	26.0 ± 0.6	normal mantle
45	ESK	55.32	−3.20	246	1	-	69.2 ± 0.2	-	normal mantle
46	FFC	54.72	−101.98	269	1	43.5 ± 0.3	68.2 ± 0.1	24.8 ± 0.3	normal mantle
47	FRB	63.75	−68.55	152	1	43.2 ± 0.4	67.2 ± 0.1	24.0 ± 0.4	normal mantle
48	FURI	8.90	38.69	226	1	49.8 ± 0.4	74.0 ± 0.2	24.2 ± 0.4	normal mantle
49	GAR	39.00	70.32	37	2	43.2 ± 0.7	71.5 ± 1.6	28.3 ± 1.7	subduction
50	GRFO	49.69	11.22	211	1	46.1 ± 0.2	69.0 ± 0.3	22.9 ± 0.3	hotspot
51	GVD	34.84	24.09	26	1	44.0 ± 1.1	65.2 ± 0.7	21.2 ± 1.3	subduction
52	HIA	49.27	119.74	139	1	46.9 ± 0.7	69.0 ± 0.1	22.1 ± 0.8	normal mantle
53	HKT	29.96	−95.84	75	2	41.7 ± 0.2	69.9 ± 0.5	28.2 ± 0.6	normal mantle
54	HLG	54.18	7.88	75	1	40.7 ± 0.2	69.0 ± 0.3	28.3 ± 0.3	normal mantle
55	HNR	−9.43	159.95	116	2	-	69.7 ± 0.3	-	subduction
56	HRV	42.51	−71.56	169	1	47.6 ± 0.4	69.4 ± 0.3	21.8 ± 0.5	normal mantle
57	HYB	17.42	78.55	323	1	47.9 ± 0.2	67.8 ± 0.1	19.9 ± 0.2	normal mantle
58	IBBN	52.31	7.76	31	1	44.6 ± 0.2	67.0 ± 0.8	22.5 ± 0.8	hotspot
59	INCN	37.48	126.63	313	1	45.8 ± 0.6	69.7 ± 0.4	24.0 ± 0.7	subduction
60	INK	68.31	−133.52	254	1	42.9 ± 0.4	67.4 ± 0.1	24.6 ± 0.4	normal mantle
61	INU	35.35	137.03	333	1	43.2 ± 0.1	70.9 ± 0.1	27.7 ± 0.1	subduction
62	ISP	37.84	30.51	134	1	44.9 ± 0.3	71.7 ± 0.8	26.9 ± 0.9	subduction
63	JER	31.77	35.20	113	1	46.5 ± 0.2	69.8 ± 0.3	23.3 ± 0.3	normal mantle
64	JOHN	16.73	−169.53	52	2	43.7 ± 1.5	67.9 ± 0.2	24.2 ± 1.5	normal mantle
65	KBS	78.93	11.94	362	1	43.2 ± 0.5	70.2 ± 0.3	27.0 ± 0.6	normal mantle
66	KEV	69.76	27.01	437	1	43.9 ± 0.1	66.8 ± 0.1	22.9 ± 0.1	normal mantle
67	KIEV	50.69	29.21	212	1	43.1 ± 0.3	67.0 ± 0.3	23.9 ± 0.4	normal mantle
68	KIP	21.42	−158.01	336	1	48.3 ± 0.3	71.0 ± 0.1	22.7 ± 0.3	hotspot
69	KIV	43.96	42.69	567	1	48.2 ± 0.1	69.7 ± 0.1	21.4 ± 0.2	normal mantle
70	KMBO	−1.13	37.25	102	1	48.7 ± 0.2	71.0 ± 0.6	22.3 ± 0.6	normal mantle
71	KONO	59.65	9.60	455	1	44.0 ± 0.1	68.0 ± 0.2	24.0 ± 0.2	normal mantle
72	KSDI	33.19	35.66	62	1	45.5 ± 0.4	72.0 ± 0.8	26.5 ± 0.9	normal mantle
73	KURK	50.72	78.62	204	1	41.5 ± 0.3	68.2 ± 0.2	26.8 ± 0.4	normal mantle

Table 1. (continued)

	Station	Lat, °	Lon, °	Number	Quality	t_{P410s}, s	t_{P660s}, s	Δt, s	Context
74	KWP	49.63	22.71	66	2	44.0 ± 0.3	68.5 ± 0.6	24.6 ± 0.6	normal mantle
75	LBTB	−25.02	25.60	103	1	43.3 ± 0.6	66.8 ± 0.5	23.4 ± 0.7	normal mantle
76	LLLB	50.61	−121.88	171	2	43.0 ± 0.9	66.8 ± 0.3	23.8 ± 0.9	normal mantle
77	LSA	29.70	91.15	177	2	44.6 ± 0.1	69.2 ± 0.1	24.6 ± 0.2	normal mantle
78	LSZ	−15.28	28.19	161	1	42.6 ± 0.5	67.0 ± 0.2	24.4 ± 0.6	normal mantle
79	LVZ	67.90	34.65	307	1	44.3 ± 0.1	67.7 ± 0.3	23.4 ± 0.3	normal mantle
80	LZH	36.09	103.84	138	1	44.4 ± 0.1	70.2 ± 0.3	25.9 ± 0.3	normal mantle
81	MAHO	39.90	4.27	76	1	47.6 ± 0.5	71.9 ± 0.3	24.3 ± 0.5	normal mantle
82	MAKZ	46.81	81.98	260	1	43.2 ± 0.1	68.2 ± 0.1	25.0 ± 0.2	normal mantle
83	MALT	38.31	38.43	95	1	45.0 ± 0.3	70.4 ± 0.2	25.4 ± 0.4	normal mantle
84	MBAR	−0.60	30.74	73	1	44.9 ± 0.9	69.8 ± 0.3	24.9 ± 0.9	normal mantle
85	MBO	14.39	−16.95	21	1	45.5 ± 0.2	69.9 ± 0.2	24.4 ± 0.3	normal mantle
86	MBWA	−21.16	119.73	135	1	-	67.8 ± 0.2	-	normal mantle
87	MDJ	44.62	129.59	165	1	45.8 ± 0.3	71.8 ± 0.2	26.0 ± 0.3	subduction
88	MELI	35.29	−2.94	55	2	47.2 ± 0.4	70.1 ± 1.4	22.9 ± 1.4	normal mantle
89	MHV	54.96	37.77	162	1	42.8 ± 0.2	67.3 ± 0.1	24.5 ± 0.3	normal mantle
90	MIDW	28.22	−177.37	60	1	46.1 ± 0.6	69.2 ± 0.7	23.1 ± 0.9	normal mantle
91	MORC	49.78	17.54	195	1	46.8 ± 1.3	72.2 ± 0.3	25.4 ± 1.4	normal mantle
92	MPG	5.11	−52.64	24	1	43.7 ± 0.9	67.9 ± 1.4	24.2 ± 1.6	normal mantle
93	MRNI	33.12	35.39	26	2	46.8 ± 0.4	71.3 ± 0.4	24.5 ± 0.6	normal mantle
94	NIL	33.65	73.27	245	1	42.8 ± 0.4	68.0 ± 0.2	25.3 ± 0.4	subduction
95	NNA	−11.99	−76.84	94	1	45.3 ± 0.4	70.8 ± 1.0	25.5 ± 1.1	subduction
96	NOUC	−22.10	166.30	114	2	45.4 ± 0.2	71.3 ± 0.7	25.9 ± 0.7	subduction
97	NRIL	69.50	88.44	92	1	43.5 ± 0.3	68.0 ± 0.2	24.5 ± 0.3	normal mantle
98	NWAO	−32.93	117.23	216	1	45.2 ± 0.2	67.0 ± 0.8	21.8 ± 0.9	normal mantle
99	OBN	55.11	36.57	678	1	42.5 ± 0.1	66.4 ± 0.1	23.9 ± 0.1	normal mantle
100	OTAV	0.24	−78.45	44	1	47.2 ± 0.8	72.0 ± 0.8	24.8 ± 1.1	subduction
101	PAB	39.55	−4.35	216	1	44.2 ± 1.4	68.8 ± 0.5	24.6 ± 1.5	normal mantle
102	PAF	−49.35	70.21	90	1	47.7 ± 0.6	70.1 ± 0.2	22.4 ± 0.6	hotspot
103	PALK	7.27	80.70	141	1	45.7 ± 0.8	69.0 ± 0.9	23.3 ± 1.2	normal mantle
104	PEL	−33.15	−70.68	56	1	44.2 ± 0.2	69.7 ± 0.3	25.4 ± 0.3	subduction
105	PET	53.02	158.65	339	1	43.1 ± 0.3	70.7 ± 0.3	27.6 ± 0.4	subduction
106	PFO	33.61	−116.46	413	1	46.1 ± 0.4	70.9 ± 0.1	24.8 ± 0.2	normal mantle
107	PMB	50.52	−123.08	71	2	46.7 ± 0.8	67.2 ± 0.8	20.5 ± 1.1	normal mantle
108	PMSA	−64.77	−64.05	131	1	49.9 ± 0.8	71.2 ± 0.4	21.4 ± 0.8	normal mantle
109	POHA	19.76	−155.53	83	1	46.8 ± 0.4	70.4 ± 0.5	23.6 ± 0.6	hotspot
110	PPT	−17.57	−149.58	143	2	47.5 ± 0.4	71.5 ± 0.3	24.0 ± 0.5	hotspot
111	PSZ	47.92	19.89	93	2	48.6 ± 0.2	69.1 ± 0.3	20.6 ± 0.4	normal mantle
112	PTCN	−25.07	−130.10	47	1	46.6 ± 0.2	69.5 ± 0.9	22.9 ± 0.9	hotspot
113	PTGA	−0.73	−59.97	25	2	44.2 ± 1.5	69.5 ± 0.9	25.2 ± 1.7	normal mantle
114	PUL	59.77	30.32	108	1	42.5 ± 0.3	66.2 ± 0.2	23.8 ± 0.3	normal mantle
115	QIZ	19.03	109.84	150	2	45.0 ± 1.0	71.8 ± 0.4	26.8 ± 1.0	normal mantle
116	QSPA	−89.93	145.00	187	1	41.6 ± 0.2	67.9 ± 0.3	26.3 ± 0.4	normal mantle
117	RAYN	23.52	45.50	240	1	45.7 ± 0.1	69.5 ± 0.6	23.8 ± 0.6	normal mantle
118	RCBR	−5.83	−35.90	97	1	45.1 ± 0.3	69.5 ± 0.5	24.4 ± 0.6	normal mantle
119	RES	74.69	−94.90	172	1	44.8 ± 0.2	69.5 ± 0.3	24.7 ± 0.3	normal mantle
120	RGN	54.55	13.32	170	1	43.6 ± 0.2	68.5 ± 0.2	24.9 ± 0.3	normal mantle
121	RPN	−27.13	−109.33	176	1	46.8 ± 0.3	70.1 ± 0.2	23.3 ± 0.3	hotspot
122	RSSD	44.12	−104.04	109	1	44.8 ± 0.3	67.8 ± 0.4	23.0 ± 0.5	normal mantle
123	RUE	52.48	13.78	115	1	44.4 ± 0.2	67.9 ± 0.2	23.5 ± 0.3	normal mantle
124	SAML	−8.95	−63.18	33	1	44.2 ± 0.7	68.3 ± 1.0	24.0 ± 1.2	normal mantle
125	SBA	−77.85	166.76	116	1	47.0 ± 0.2	70.5 ± 0.5	23.5 ± 0.6	hotspot
126	SCHQ	54.83	−66.83	123	1	43.7 ± 0.3	67.2 ± 0.2	23.5 ± 0.3	normal mantle
127	SCZ	36.60	−121.40	180	2	46.8 ± 0.1	70.5 ± 0.2	23.7 ± 0.2	normal mantle
128	SDV	8.88	−70.63	83	1	41.8 ± 0.6	68.5 ± 0.9	26.7 ± 1.1	normal mantle
129	SEY	62.93	152.37	39	1	43.8 ± 0.6	69.6 ± 0.5	25.9 ± 0.8	normal mantle
130	SFJ	67.00	−50.62	73	1	43.9 ± 0.6	67.2 ± 0.3	23.3 ± 0.6	normal mantle
131	SFJD	67.00	−50.62	57	1	43.2 ± 0.3	65.8 ± 0.4	22.6 ± 0.6	normal mantle
132	SHEL	−15.96	−5.75	100	1	46.8 ± 0.2	71.2 ± 0.5	24.4 ± 0.6	normal mantle
133	SNAA	−71.67	−2.84	61	1	44.1 ± 0.5	69.0 ± 1.0	24.9 ± 1.1	normal mantle
134	SNZO	−41.31	174.70	175	2	43.2 ± 0.4	68.0 ± 1.2	24.8 ± 1.2	subduction
135	SPB	−23.59	−47.43	23	1	45.6 ± 0.6	68.3 ± 0.6	22.7 ± 0.9	normal mantle
136	SSB	45.28	4.54	230	1	46.4 ± 0.2	71.3 ± 0.3	24.9 ± 0.3	normal mantle
137	SSE	31.10	121.19	140	2	44.1 ± 0.5	70.4 ± 0.6	26.4 ± 0.8	normal mantle
138	SSPA	40.64	−77.89	120	1	44.2 ± 0.5	67.8 ± 0.3	23.6 ± 0.6	normal mantle
139	STU	48.77	9.19	238	1	45.3 ± 0.3	68.6 ± 0.9	23.3 ± 0.9	hotspot
140	SUMG	72.58	−38.45	28	1	46.2 ± 0.4	69.0 ± 0.4	22.8 ± 0.6	normal mantle
141	SUR	−32.38	20.81	199	1	-	67.8 ± 0.2	-	normal mantle
142	SUW	54.01	23.18	204	1	44.0 ± 0.7	67.3 ± 0.2	23.3 ± 0.7	normal mantle
143	SYO	−69.01	39.58	94	1	44.9 ± 0.5	67.4 ± 0.3	22.5 ± 0.6	normal mantle
144	TAM	22.79	5.53	107	1	47.6 ± 0.6	71.0 ± 0.3	23.4 ± 0.7	hotspot
145	TAU	−42.91	147.32	178	1	46.1 ± 0.4	68.9 ± 0.3	22.8 ± 0.5	normal mantle
146	TEIG	20.23	−88.28	31	2	44.1 ± 1.1	70.2 ± 0.3	26.1 ± 1.1	normal mantle

Table 1. (continued)

	Station	Lat, °	Lon, °	Number	Quality	t_{P410s}, s	t_{P660s}, s	$\Delta\,t$, s	Context
147	TIRR	44.46	28.41	65	1	44.2 ± 0.3	68.0 ± 0.7	23.8 ± 0.8	normal mantle
148	TIXI	71.65	128.87	197	1	43.1 ± 0.2	66.4 ± 0.1	23.3 ± 0.2	normal mantle
149	TLY	51.68	103.64	440	1	46.6 ± 0.3	69.9 ± 0.1	23.3 ± 0.3	normal mantle
150	TRTE	58.38	26.72	70	1	42.2 ± 0.7	66.5 ± 0.6	24.2 ± 0.9	normal mantle
151	TSK	36.21	140.11	105	1	46.5 ± 0.9	68.0 ± 0.4	21.6 ± 1.0	subduction
152	TSUM	−19.20	17.58	147	1	43.9 ± 0.2	68.7 ± 0.1	24.8 ± 0.2	normal mantle
153	TUC	32.31	−110.78	261	1	47.2 ± 0.1	71.2 ± 0.2	24.0 ± 0.2	normal mantle
154	ULN	47.87	107.05	267	1	44.3 ± 0.1	69.5 ± 0.1	25.1 ± 0.2	normal mantle
155	UNM	19.33	−99.18	81	2	47.5 ± 0.2	70.9 ± 0.6	23.4 ± 0.6	subduction
156	VNDA	−77.52	161.85	118	2	46.7 ± 0.5	68.0 ± 0.8	21.4 ± 0.9	hotspot
157	VSU	58.46	26.73	72	1	42.8 ± 0.1	66.4 ± 0.3	23.7 ± 0.3	normal mantle
158	WCI	38.23	−86.29	52	1	42.8 ± 0.6	69.0 ± 0.3	26.2 ± 0.7	normal mantle
159	WHY	60.66	−134.88	261	1	48.2 ± 0.2	70.2 ± 0.3	22.1 ± 0.4	normal mantle
160	WLF	49.66	6.15	171	1	-	71.6 ± 0.4	-	hotspot
161	WMQ	43.82	87.69	199	1	40.2 ± 0.4	69.0 ± 0.2	28.8 ± 0.4	normal mantle
162	WRAB	−19.93	134.36	237	1	42.8 ± 0.2	67.3 ± 0.2	24.5 ± 0.2	normal mantle
163	WUS	41.20	79.22	194	1	43.3 ± 0.3	70.0 ± 0.3	26.6 ± 0.4	normal mantle
164	WVT	36.13	−87.83	51	1	43.9 ± 0.7	68.2 ± 0.3	24.4 ± 0.7	normal mantle
165	YAK	62.03	129.68	460	1	43.1 ± 0.2	66.9 ± 0.1	23.9 ± 0.2	normal mantle
166	YKW3	62.56	−114.61	248	1	43.4 ± 0.2	68.5 ± 0.2	25.1 ± 0.2	normal mantle
167	YSS	46.96	142.76	411	1	43.7 ± 0.3	69.3 ± 0.2	25.6 ± 0.3	subduction

From left to right: station number (see Figure 1 for locations), latitude, longitude, number of stacked receiver functions, data quality, absolute travel times for the $P410s$ (t_{P410s}) and $P660s$ (t_{P660s}) phases, differential t_{P410s}- t_{P660s} ($\Delta\,t$) travel times, and the "a priori" tectonic province.

the distribution of seismic heterogeneities in the DKP2005 [*Debayle et al.*, 2005] seismic model to correct for absolute travel times and obtain a more reliable estimation of the 410-km discontinuity depth.

[26] We first produce average 1D shear wave speed profiles beneath each station in DKP2005. We average at each depth, in the top 400 km of the tomographic model, the lateral variations in shear velocity taken in a circular region centered on the station and with a radius of 200 km. This allows us to take into account the area covered by the

piercing point of the $P410s$ phases (see Figure 2). We predict the $P410s$ arrival times for a shallow earthquake recorded at a distance of 65°, by ray-tracing through the average 1D S-wave profiles and the 20 s period PREM P wave velocity distribution. The time residual between the arrival time predicted by the 1D S-wave profile and IASP91 provides a time correction. We tried different P wave velocity models, starting with PREM at 20 s period, and adding P wave perturbations δV_P linearly related to the S-wave perturbations δV_S using scaling factors ($\delta V_S/\delta V_P$)
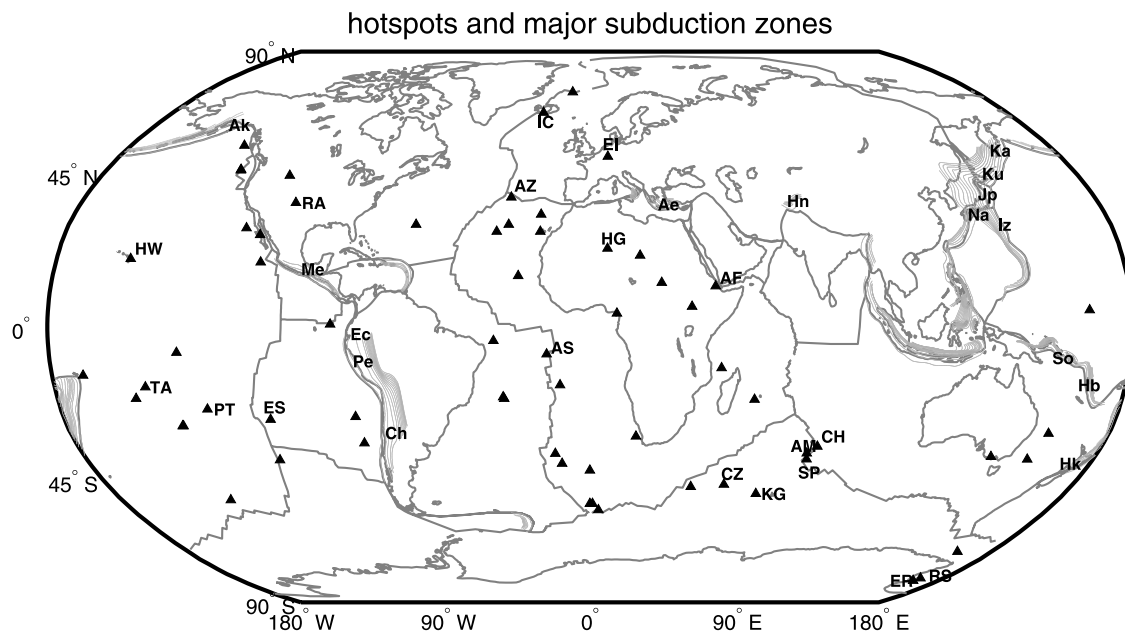

Figure 6. Hotspot and subduction zone locations used to define the "subduction", "hotspot", and "normal mantle" MTZ provinces. Hotspot locations from a compilation by *Anderson and Schramm* [2005] are shown with black triangles. Depth isolines in gray indicate the top of slabs after the RUM model [*Gudmundsson and Sambridge*, 1998]. Labels used for hotspot and subduction segments refer to Table 2.

Table 2. List of Hotspot and Subduction Segments With Associated Abbreviations[a]

Abs.	Hotspots Names	Stations	Abs.	Subductions Names	Stations
AF	Afar	ATD	Ae	Aegean	GVD ISP
AM	Amsterdam	AIS	Hn	Hindu	GAR NIL
AS	Ascension	ASCN	Na	Nankai	INCN INU
AZ	Azores	CMLA	Hk	Hikurangi	SNZO
CH	Christmas	AIS	Hb	New Hebrides	DZM NOUC
CZ	Crozet	CRZF	So	Solomon	HNR
ES	Easter	RPN	Iz	Izu-Bonin	INU TSK
EI	Eifel	BFO ECH GRFO	Jp	Japan	INU TSK
		IBBN STU WLF	Ku	Kurile	YSS
HW	Hawaii	KIP POHA	Ka	Kamchatka	PET
HG	Hoggar	TAM	Ak	Alaska	COL COLA
IC	Iceland	BORG	Me	Mexico	UNM
ER	Mount Erebus	SBA VNDA	Ec	Ecuador	OTAV
PT	Pitcairn	PTCN	Pe	Peru	NNA
RA	Raton New Mexico	ANMO	Ch	Central Chile	PEL
RS	Ross Sea	SBA VNDA			
SP	St Paul	AIS			
TA	Tahiti	PPT			

[a]The name of the stations associated with each hotspot and subduction segments are also provided.

ranging between 1.5 and 4. We found that the choice of the P wave model has little effect on the predicted t_{P410s} arrival times. We also tried the S-wave model of *Ritsema et al.* [1999] with the same range of P wave models as for DKP2005. We found very similar results.

[27] These time corrections are equivalent to a time-to-depth migration. We have performed the time-to-depth migration using the S and P wave velocity distribution of (1) IASP91; (2) PREM at 20 s period; (3) a model made by DKP2005 for the S-wave distribution and PREM at 20 s period for the P wave velocity. Corrected depths for the 410 km are shown for the normal mantle (Figure 11a), subduction (Figure 11b) and hotspots (Figure 11c) subsets of stations. The apparent 410-km depth curves obtained for the normal mantle are roughly symmetrical with respect to the standard depth of 410 km (Figure 11a). For the subduction province, about two thirds of the stations display a shallower 410-km discontinuity (Figure 11b) and this proportion increases to 80% if we consider only the stations with error bars smaller than 5 km. The most striking result is observed for hotspots, where the 410-km discontinuity depth is deflected downward beneath a large majority of the stations (Figure 11c).

4. Discussion

4.1. Anomalous Observations and Error Measurements

[28] Some of the stacks shown in Figure 5 display complicated waveforms. For instance, we observe two peaks around the time of the $P410s$ arrival at stations GVD, INU, PEL and WMQ. The obtained MTZ thicknesses and apparent discontinuity depths depend on the choices made when selecting the peaks. We checked that at each of these stations, choosing another peak would produce unrealistic apparent depths for the 410-km discontinuity. We also carefully checked the consistency of the receiver functions using sections such as the ones shown in Figure 3, sorted by back-azimuth or epicentral distance. We believe
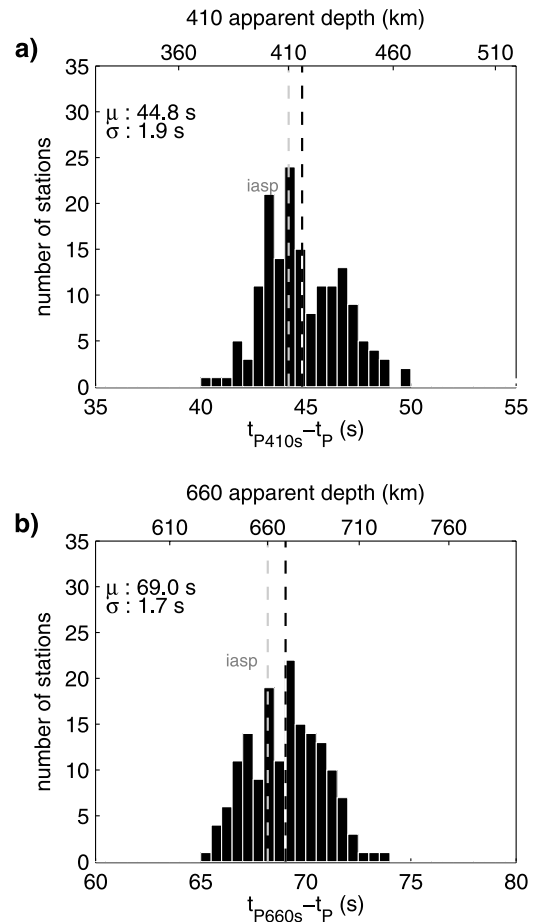

Figure 7. Global distribution of our absolute (a) $P410s$ and (b) $P660s$ arrival times. Arrival times in IASP91 are shown with grey dashed lines. The vertical black dashed lines indicate the position of the average values μ, which are given with their standard deviations σ at the top left of each figure. Histograms are built using bins of 0.5 s width. The absolute depth in IASP91 is given at the top of each panel.
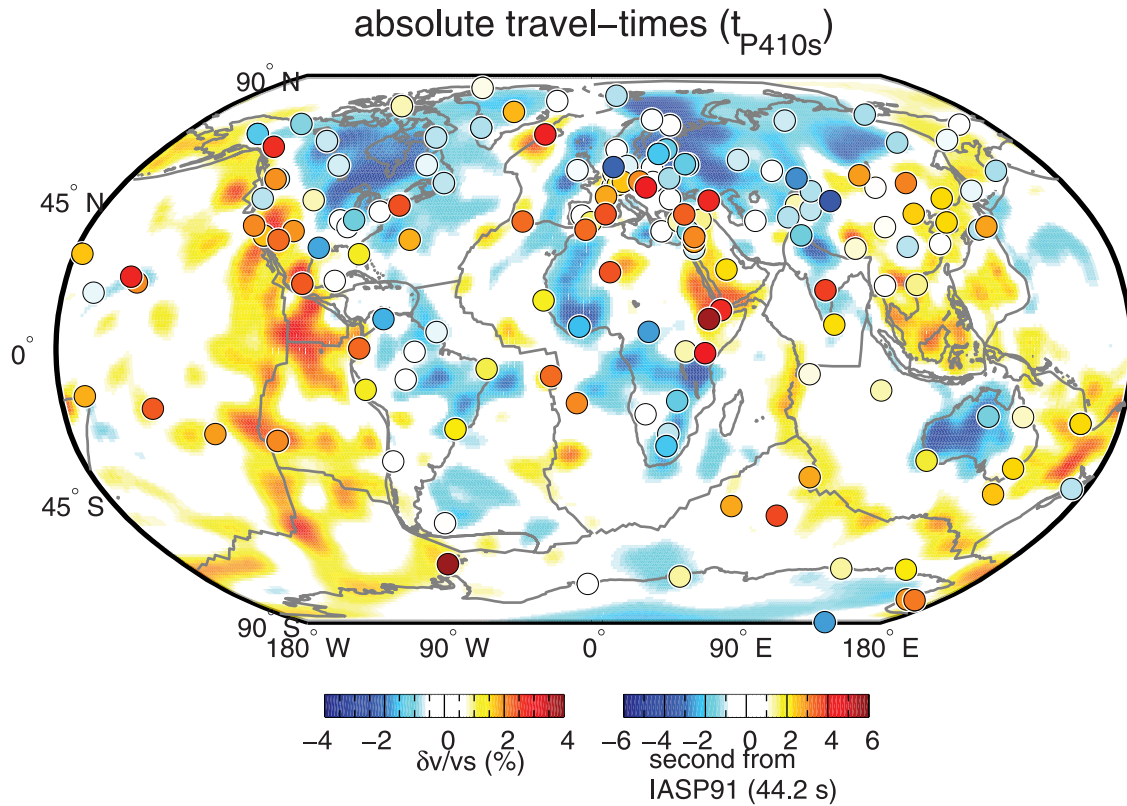
absolute travel–times (t_{P410s})

Figure 8. Travel-time residuals ($tP_{410}s$ observed minus $tP_{410}s$ predicted by IASP91) are superimposed on a map showing the vertical average of S-wave velocity anomalies above the MTZ in DKP2005 [*Debayle et al.*, 2005]. The color scale within circles is for the travel-time residuals, while the background color scale indicates lateral perturbations in S-wave velocities.

our selected peaks are the most likely to correspond to the $P410s$ or $P660s$ waveforms.

[29] Standard errors on our travel-time measurements are estimated using a bootstrap resampling approach [*Efron and Tibshirani*, 1991] and are given in Table 1. They range from 0.1 s (∼1 km) to about 1.5 s (∼15 km). The mean value is 0.5 s (∼5 km). Errors larger than 1 s have been found at 24 stations, 2 of them belonging to the hotspot group (ASCN and CRZF), 7 to the subduction group (DZM, GAR, GVD, NNA, OTAV, SNZO and TSK) and 15 to the normal mantle group of stations (COR, DAG, DWPF, JOHN, MELI, MORC, MPG, PAB, PALK, PMB, PTGA, SAML, SDV, SNAA and TEIG). These large errors may be due to the weak number of stacked data or to strong 3D heterogeneities or topography variations beneath the station. They suggest that the travel times should be interpreted with cautions.

[30] Stations PET, YSS and HYB have broad $P410s$ peaks and small errors. These small errors mean that the travel times are weakly sensitive to the selected bootstrap sample and correspond to features that are common to most receiver functions at these stations. However, a broad peak may indicate that the waveform complexity has not entirely been taken into account in the error estimation, and this should be kept in mind when interpreting the travel times at these stations.

[31] We did not measure the t_{P410s} travel times and associated errors at stations showing broad $P410s$ peaks

and very weak or null $P410s$ amplitudes (ESK, HNR, MBWA, SUR, WLF).

[32] Some stations are therefore associated with significant waveform complexity and travel-time errors. For this reason, we do not interpret individual travel times in the following sections of this paper. Instead, we focus on the robust tendencies that can be extracted from our 167 stations.

4.2. Average MTZ Thickness

[33] In IASP91, the 24 s average differential travel time found in CVM99 is compatible with a MTZ average thickness very close to 250 km. LS06 pointed out a 8 km discrepancy between this value and results of SdS studies by *Flanagan and Shearer* [1998] or *Gu and Dziewonski* [2002]. They suggested that the discrepancy between Pds and SdS studies is due to the limited geographic sampling of Pds measurements and the constant ray parameter approximation used in CVM99.

[34] To allow a direct comparison between CVM99, LS06 and our differential travel-time measurements (hereafter referred as TDW08), we converted CVM99 and TDW08 travel times into MTZ thicknesses using the PREM model at 20 s period [*Dziewonski and Anderson*, 1981]. The obtained MTZ thicknesses are consistent with the uncorrected values obtained by LS06 and are displayed on Figures 12a, 12b and 12c.
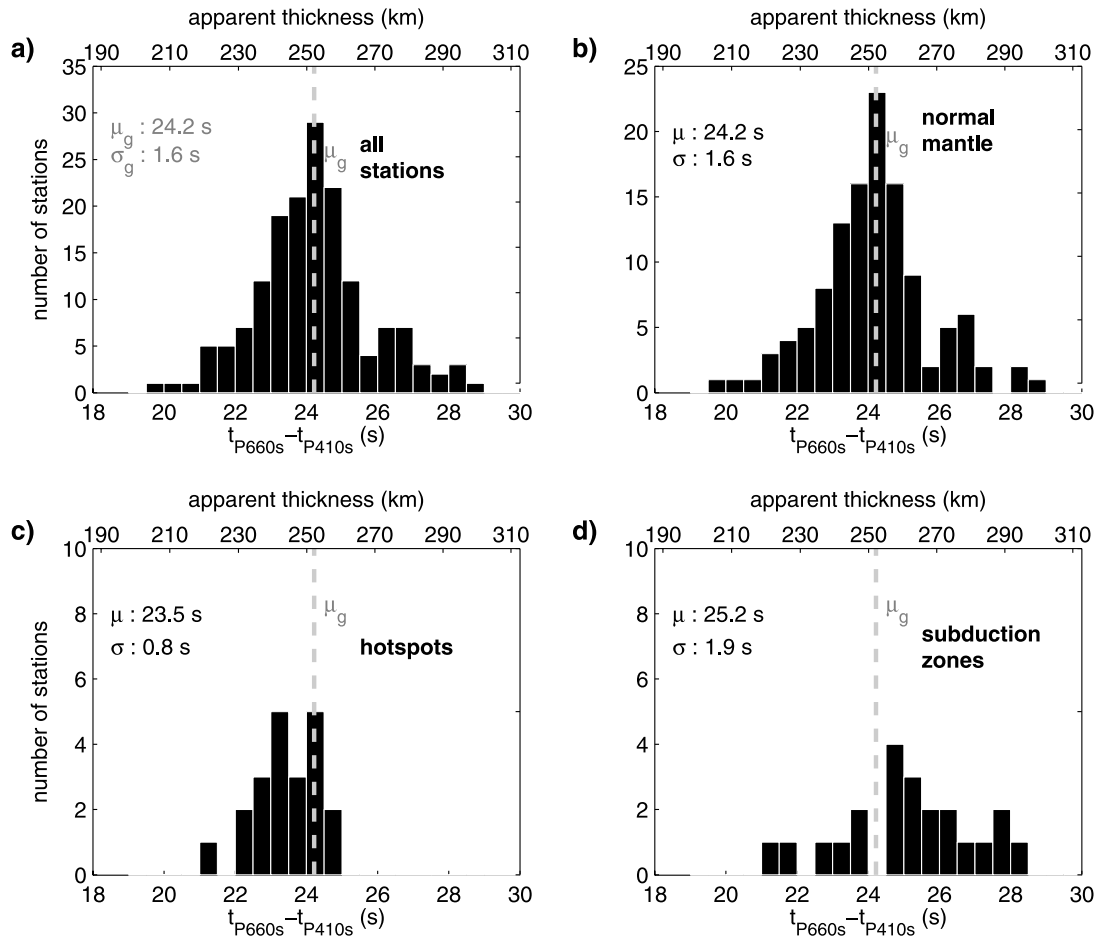
Figure 9. Distributions of differential travel times $t_{P660s} - t_{P410s}$ for (a) all our quality 1 and 2 stations, (b) the "normal mantle" subset of stations, (c) the "hotspot" subset of stations, and (d) the "subduction" subset of stations. Average and standard deviations are indicated at the top left of each panel. The grey dashed lines indicate the position of the global average ($\mu_g = 24.2$ s). Histograms are made with 0.5 s bins ranging from 18 s to 30 s. The apparent MTZ thickness in IASP91 is given at the top of each panel.

[35] The CVM99 average MTZ thickness reduces to 243 km and provides now the best agreement with SS-precursor studies (242 km in *Flanagan and Shearer* [1998]; *Gu and Dziewonski* [2002]). This clearly demonstrates that the global average thickness is strongly influenced by the velocity model, as well as by the constant ray parameter approximation.

[36] Both LS06 and our study agree on a thicker average MTZ of 247 km, but as in LS06, we do not consider that this is inconsistent with SS-precursor studies. As *Pds* waves preferentially sample the thick MTZ of continents, they are likely to provide an upper bound for the MTZ thickness [*Gu and Dziewonski*, 2002].

4.3. Lateral Variations in MTZ Thickness

[37] Figures 12a, 12b, and 12c reveal another striking difference between CVM99 observations and the two other studies. TDW08 and LS06 show an overall agreement for the lateral variations in MTZ thickness, with typical amplitudes of ±20 km and maximal variations reaching ±35−40 km in both studies. In contrast, the observed variations are much weaker in CVM99 and stay within ±10 km of the

global average, except for two noisy stations in the South Pacific (PPT and RAR).

[38] As noticed by *Lawrence and Shearer* [2006], one part of the discrepancy may be attributed to the different sampling of the Earth. *Chevrot et al.* [1999] use essentially continental stations, in general far from the influence of major subduction zones and hotspots. In CVM99, only 11 stations belong to the "subduction" province against 22 in LS06 and 24 in TDW08. In addition, 8 stations of CVM99 belong to the "hotspot" province against 12 in LS06 and 22 in TDW08.

[39] However, significant differences remain at stations that are common to CVM99 and the two other studies, and the repartition of stations cannot explain all the observed discrepancies. Figure 13 compares the observed MTZ thicknesses for the stations common to TDW08 and CVM99 (48 stations), TDW08 and LS06 (73 stations), and LS06 and CVM99 (28 stations). Although there is a reasonable correlation between TDW08 and LS06, the correlation between CVM99 and the two other studies is weak or null, except for a small number of stations.

[40] Finding the cause of these differences is difficult, as a number of factors influence the MTZ thickness observa-
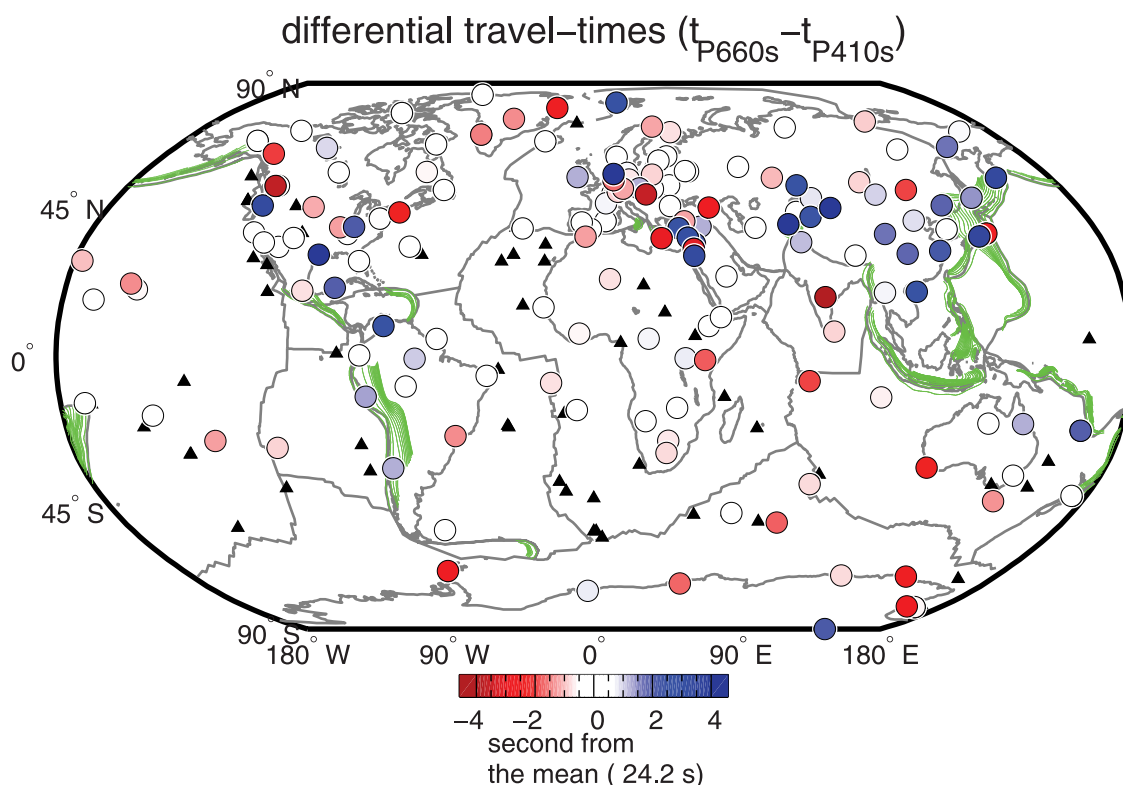
differential travel−times ($t_{P660s} − t_{P410s}$)

Figure 10. Differential travel-time anomalies relative to the global average (24.2 s) superimposed to the hotspot and subduction locations.

tions (number of data, repartition in back azimuth, quality and frequency content). We assume the most significant part of the discrepancy comes from the number of data, as the two most recent studies by LS06 and TDW08 include a much larger number of data compared to CVM99. For instance, the average number of receiver functions stacked per station is around 163 in our study against 55 in CVM99.

4.4. Observations Beneath Normal Mantle Stations

[41] The normal MTZ subset of stations shows up with the largest scatter in MTZ thickness (Figure 9b), suggesting that significant variations of the discontinuity topography and/or transition zone wave speeds are present away from subductions and hostposts. At least 40% of our "normal MTZ" measurements differ by more than ±1 s from IASP91, suggesting that what we call the "normal MTZ" region is in fact an heterogeneous region. Our coarse a priori regionalization assumes that the mantle is unperturbed away from active slabs and hotspots, without considering the effect of other heterogeneities such as fossil subduction zones, stagnant slabs, or plumes that may not have reached the surface. It is for example possible that the fossil Farallon subduction contributes to the NW–SE pattern of thick MTZ observed beneath the normal MTZ stations of north and central America (Figure 10).

4.5. Observations Beneath Subduction Stations

[42] Two thirds of the "subduction" stations have an anomalously large MTZ thickness (Figure 9d). The MTZ thickness can be converted in a thermal anomaly, assuming that this anomaly is constant within the transition zone and

that seismic heterogeneities within the MTZ can be neglected. We use Clapeyron slopes of +3 MPa/K and −3 MPa/K for the "410" and the "660" respectively. These values are in the range of previous published values, 1.5 to 3.5 MPa/K for the 410-km and −4.0 to −2.0 MPa/K for the 660-km discontinuities [*Akaogi et al.*, 1989; *Suito*, 1977; *Ito et al.*, 1990; *Bina and Helffrich*, 1994].

[43] Using these assumptions, we found that under half of the subduction stations (NIL, PEL, NNA, YSS, NOUC, MDJ, DZM, ISP, CSS, PET, INU and GAR), the MTZ thickness is compatible with a thermal anomaly ranging between −100° and −300°K (Figure 5).

[44] We then require the obtained thermal anomaly to be compatible with the "410" apparent topography, in addition to be compatible with the apparent MTZ thickness. The number of stations fitting both conditions reduces to 7: the observed MTZ thickness (Table 1) and "410" apparent depth of stations INU, PET, CSS, YSS, PEL, SNZO and NIL can be explained by a single thermal anomaly ranging between −100° and −300°K. At other stations, the MTZ thickness and the "410" apparent depth are more difficult to interpret with a single thermal anomaly. Stations COL and COLA in Alaska and CHTO in Thailand show a normal MTZ thickness but an uplifted 410-km discontinuity. In these regions the slab may not have reached the bottom of the transition zone [*Replumaz et al.*, 2004; *Qi et al.*, 2006]. Cases where the MTZ is clearly thickened, with the major part of the topography restricted to the "660" (ISP in Aegea, NOUC and DZM for New Hebridies, GAR for Hindu and MDJ for Japan subduction zones) are more difficult to explain. It is likely that our assumption that
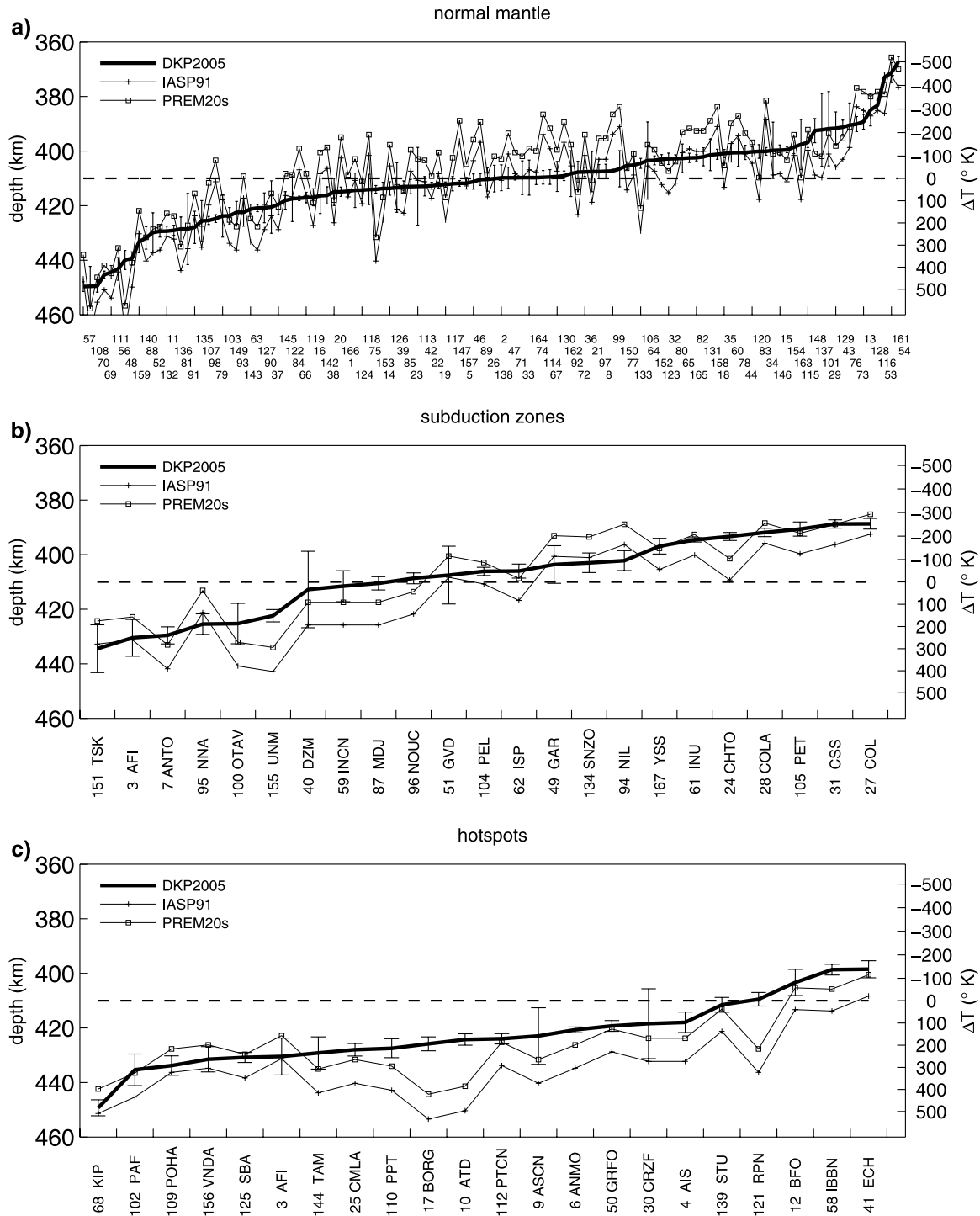
Figure 11. Topography of the 410-km depth discontinuity for (a) the "normal mantle" subset of stations, (b) the "subduction" subset of stations, and (c), the "hotspot" subset of stations. DKP2005 [*Debayle et al.*, 2005], IASP91, and PREM 20s velocity models were used to convert arrival times into depth. Stations are sorted by order of decreasing depths after migration in DKP2005. The horizontal black dashed line marks the reference depth of the 410-km discontinuity in IASP91. Right y-axis gives thermal perturbations expected for depths given on the left y-axis and using a +3 MPa/K Clapeyron slope. The numbers on the x-axis refer to stations in Table 1.
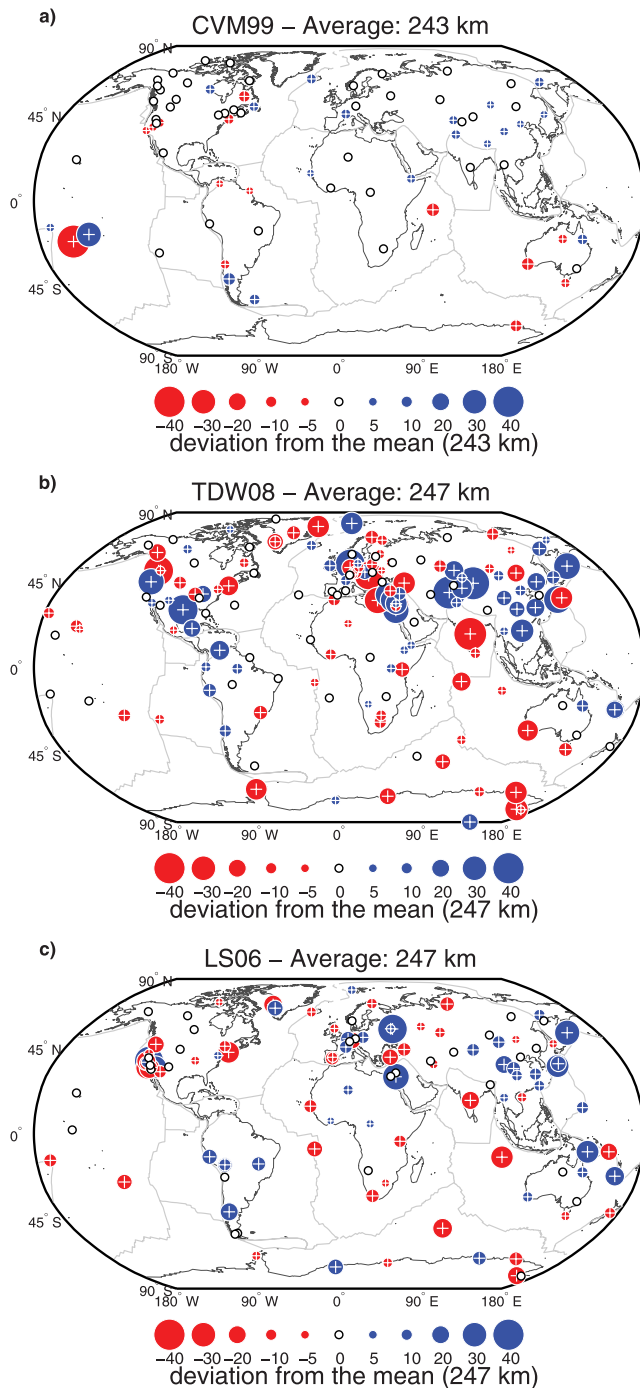
Figure 12. MTZ thickness variations after depth migration in the PREM model at 20 s period [*Dziewonski and Anderson*, 1981] for (a) the *Chevrot et al.* [1999] data set, (b) this study, and (c) the *Lawrence and Shearer* [2006] data set. Radii of the dots linearly depend on the perturbation from the global average of each study. Blue is for a thick MTZ; red is for a thin MTZ.

the structure does not vary laterally beneath the station is more restrictive beneath subduction stations where strong 3D heterogeneities are likely to be present. This could also explain the relatively large measurement errors (>0.7 s)

observed at stations DZM, GAR, GVD, INCN, ISP, NNA, NOUC, TSK and OTAV.

[45] Our observations of MTZ thicknesses (Figure 9c) and 410-km apparent topography (Figure 11b) suggest that at least in some cases, deep cold slabs affect the topography of the 410- and 660-km discontinuities in a way which is consistent with the Clapeyron slopes of olivine. However, large uncertainties remain on the effect of 3D seismic heterogeneities located within and above the transition zones, and it is difficult to estimate accurately the corresponding temperature anomalies.

4.6. Observations Beneath Hotspots

[46] In general, the "410" corrected depth under hotspots remains at least 10 km deeper than in the IASP91 model, with the exception of few continental stations (BFO, ECH, IBBN, STU) neighboring the Eifel hotspot and the oceanic station RPN near the Easter hotspot (Figure 11c). L03 made a similar observation using a lower frequency data set of P-to-Sv converted waves, but without applying corrections for 3D upper mantle or crustal structure.

[47] In our case, the uncorrected depths predict thermal perturbations ranging from +300°K to more than 500°K. After 3D velocity corrections, we obtain a more realistic distribution of thermal anomalies at 410-km depth, ranging from +100° to +300°K. For this range of thermal perturbations, pressure-temperature dependence of olivine phase transformations should produce a 15–40 km thinning of the MTZ. However, a deep apparent 410-km discontinuity is not always associated with a thin MTZ in our observations. Indeed, for most of the "hostpot" stations, the apparent MTZ thickness ranges within ±10 km of the 250 km of IASP91 (±1 s of the 24 s of IASP91, Figure 9c).

[48] Several scenarios can be invoked to reconcile our apparent 410-km discontinuity depths and the MTZ thicknesses. Some of the hot anomalies observed near 410-km depth may not be continuous throughout the MTZ down to the 660-km discontinuity. However, mantle plumes are thought to originate from a thermal boundary layer, and it is difficult to imagine that such plumes can originate somewhere between the 410-km and 660-km discontinuities, especially as some observations of deep apparent 410-km and 660-km discontinuities (e.g., ATD, BORG, PPT, TAM, Table 1) require strong cold anomalies at 660 km, of the order of what would be expected for cold subducted material.

[49] A second explanation may come from our velocity corrections. As we do not correct for velocity heterogeneities within the MTZ, our estimated thickness will be biased toward thicker values if a slow velocity anomaly is present within the MTZ. We may also underestimate the t_{P410s} correction if we underestimate the amplitude of slow velocity perturbations above the MTZ. It is therefore possible that our imperfect knowledge of the 3D distribution of seismic heterogeneities within the upper mantle is responsible for at least part of the observed discrepancy between our differential and absolute travel times.

[50] In the next section, we explore an other alternative, in the light of recent results of mineral physics.

4.7. Effect of the Majorite-Perovskite Phase Transition

[51] The α to β transition and the postspinel transformation in olivine are generally believed to be responsible for

a)

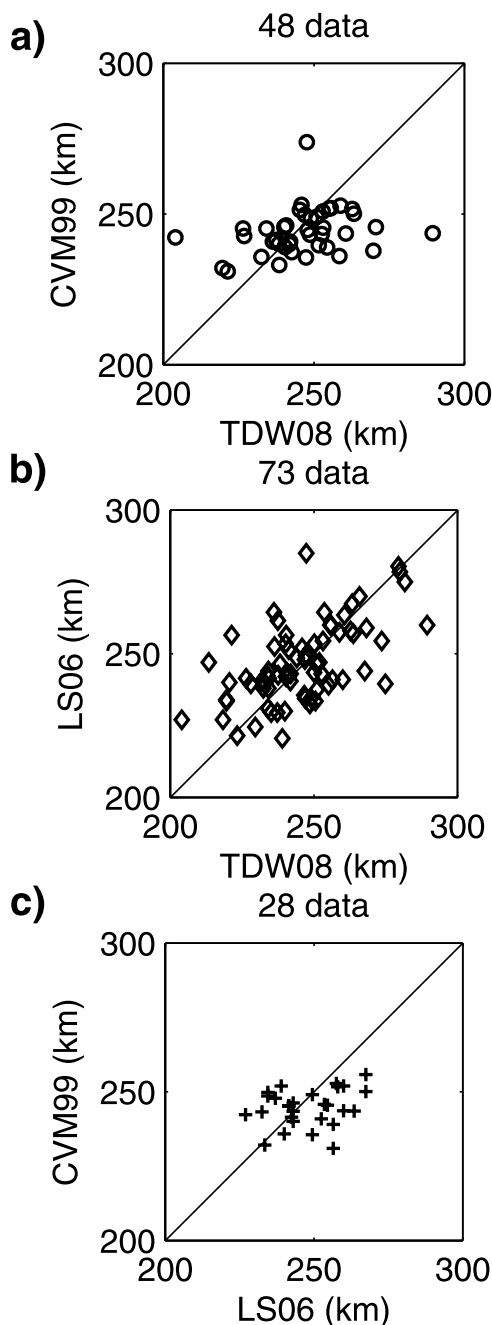## 48 data

b)

73 data

c)

28 data

Figure 13. Correlation plots between MTZ thicknesses obtained by *Chevrot et al.* [1999] (CVM99), *Lawrence and Shearer* [2006] (LS06), and this study (TDW08): (a) CVM99 versus TDW08 thicknesses, (b) LS06 versus TDW08 thicknesses, and (c) CVM99 versus LS06 thicknesses. Differential travel times were converted into depths in PREM at 20 s period [*Dziewonski and Anderson*, 1981].

the observed 410-km and 660-km seismic velocity discontinuities in the mantle. An elevation of the 660-km boundary is thus expected in regions with high mantle temperatures.

[52] However, another major component of the mantle, majorite garnet, may also transform into perovskite at around 660-km depth. At high temperatures (above 2100°K, +200° to +300°K higher than the global average), this phase

transition is found at 660-km depth with a positive Clapeyron slope (+1.3 MPa K^{-1}) [*Hirose*, 2002] which would imply a deepening of the reaction with increasing temperatures. The majorite garnet and postspinel phase transitions occur at similar depths, so that the observed seismic discontinuity could be caused by a combination of both phase transitions [*Hirose*, 2002]. A broad (30 km thick) velocity discontinuity may result from this combination but would still convert sufficient energy to be detected by our long period data set (>10 s period). If the positive Clapeyron slope of the majorite garnet transformation counterbalances the negative Clapeyron slope of the postspinel transformation within high-temperature plumes, the depth of the 660-km discontinuity may be less temperature sensitive and greater [*Hirose*, 2002]. In this case, the resulting MTZ thickness variation is expected to be weak, as it depends on the difference between the 410-km and 660-km Clapeyron slopes.

[53] This is indeed what we observe: most of our 410-km apparent topography observations are compatible with thermal anomalies of an order of +200° to +300°K at 410-km depth under hotspots, but are associated to MTZ thickness variations limited to ±10 km around IASP91 (Figure 9c).

[54] If the effect of the majorite-perovskite phase transition is to reduce the MTZ thickness variations within high-temperatures plumes, the MTZ thickness may not be a suitable discriminant parameter to detect deep mantle plumes. Because the 410-km discontinuity is not affected by the majorite/garnet phase transformation, the less robust apparent depth of the 410-km discontinuity may contain important information to detect mantle plumes. Figure 11c confirms that the 410-km discontinuity is in general deflected downward beneath hotspot stations.

[55] Using SS-precursor observations beneath twenty-six hotspot locations, *Deuss* [2007] found evidence for late arrivals and deeper than average depths for the 410-km discontinuity in about two thirds of the cases. As in this study, most locations with deep 410-km discontinuities have thin or average transition zone thicknesses.

5. Conclusions

[56] We have measured travel times of *Pds* converted waves at the 410-km and 660-km discontinuities beneath 167 seismic stations. Our results extend previous work by LS06 and CVM99 with a larger data set, especially near hotspots and subduction zones.

[57] We confirm that average MTZ thicknesses derived from *Pds* and SS precursors studies are consistent, if we take into account the fact that *Pds* are likely to provide an upper bound for the MTZ thickness because they preferentially sample continental regions. After migration in the PREM model at 20 s period, we obtain as in LS06, an average MTZ thickness of 247 km slightly greater than in CVM99. It is however clear that MTZ thicknesses should be interpreted with caution, as they are strongly influenced by the velocity model used for the migration.

[58] We find significant lateral variations in the MTZ thickness, with maximal amplitudes of ±35−40 km, and a long-wavelength pattern in overall agreement with SS precursor studies. These lateral variations remain important in regions of the mantle located away from hotspots and

present subductions. We observe a NW−SE pattern of thick MTZ beneath central and north America, which suggests a thickening of the MTZ associated with the fossil Farallon subduction. The MTZ is generally found to be thick under subductions (compatible with a thermal anomaly between $-100°K$ and $-300°K$) and thin or normal beneath oceanic regions, but there is no clear evidence for a thinning of the MTZ beneath hotspots.

[59] However, although the MTZ is generally not significantly thinner beneath hotspot stations, the 410-km discontinuity remains generally deflected downward. This suggests that the depth of the 660-km discontinuity is less temperature sensitive in hot regions of the mantle, which is consistent with a phase transition from majorite garnet to perovskite at a depth of 660 km. If correct, the main effect of hot mantle plumes crossing the MTZ is expected to be observed on the topography of the 410-km discontinuity, which underlines the importance of mapping accurately its depth. Our ability to achieve an accurate mapping of the 410-km absolute topography relies on our ability to perform accurate 3D shallow velocity corrections, which is an important issue to address in future.

References

Akaogi, M., E. Ito, and A. Navortsky (1989), Olivine-modified spinel-spinel transitions in the system Mg_2SiO_4-Fe_2SiO_4: Calorimetric measurements, thermochemical calculation, and geophysical application, *J. Geophys. Res.*, *94*(B11), 15,671–15,685.

Anderson, D., and K. Schramm (2005), Global hotspot maps, in *Plates, Plumes and Paradigms*, vol. 388, edited by G. Foulger et al., pp. 19–29, Geological Society of America, Boulder, CO, doi:10.1130/2005.2388(03).

Bina, C., and G. Helffrich (1994), Phase transition Clapeyron slopes and transition zone seismic discontinuity topography, *J. Geophys. Res.*, *99*(B8), 15,853–15,860.

Chevrot, S., L. Vinnik, and J. Montagner (1999), Global-scale analysis of the mantle Pds phases, *J. Geophys. Res.*, *104*(B9), 20,203–20,219.

Debayle, E., B. Kennett, and K. Priestley (2005), Global azimuthal seismic anisotropy and the unique plate-motion deformation of Australia, *Nature*, *433*, 509–512, doi:10.1038/nature03247.

Deuss, A. (2007), Seismic observations of transition zone discontinuities beneath hotspot locations, in *Plates, Plumes, and Planetary Processes*, vol. 430, edited by G. Foulger and J. Jurdy, pp. 121–136, Geological Society of America, Boulder, CO, doi:10.1130/2007.2430(07).

Deuss, A., S. Redfern, K. Chambers, and J. Woodhouse (2006), The nature of the 660-kilometer discontinuity in earth's mantle from global observations of PP precursors, *Science*, *311*, 198–201, doi:10.1126/science.1120020.

Dziewonski, A. M., and D. Anderson (1981), Preliminary Reference Earth Model, *Phys. Earth Planet. Inter.*, *25*, 297–356, doi:10.1016/0031-9201(81)90046-7.

Efron, B., and R. Tibshirani (1991), Statistical data analysis in the computer age, *Science*, *253*(5018), 390–395, doi:10.1126/science.253.5018.390.

Flanagan, M., and P. Shearer (1998), Global mapping of topography on transition zone velocity discontinuities by stacking SS precursors, *J. Geophys. Res.*, *103*(B2), 2673–2692.

Gilbert, H. J., A. F. Sheehan, D. A. Wiens, K. G. Dueker, L. M. Dorman, J. Hildebrand, and S. Webb (2001), Upper mantle discontinuity structure in the region of the Tonga subduction zone, *Geophys. Res. Lett.*, *28*(C9), 1855–1858.

Gu, Y., and A. Dziewonski (2002), Global variability of transition zone thickness, *J. Geophys. Res.*, *107*(B7), 2135, doi:10.1029/2001JB000489.

Gu, Y., A. Dziewonski, and C. Agee (1998), Global de-correlation of the topography of transition zone discontinuities, *Earth Planet. Sci. Lett.*, *157*, 57–67.

Gudmundsson, Ó., and M. Sambridge (1998), A regionalized upper mantle (RUM) seismic model, *J. Geophys. Res.*, *103*(B4), 7121–7136.

Hirose, K. (2002), Phase transitions in pyrolitic mantle around 670-km depth: Implications for upwelling of plumes from the lower mantle, *J. Geophys. Res.*, *107*(B4), 2078, doi:10.1029/2001JB000597.

Ito, E., M. Akaogi, L. Topor, and A. Navrotsky (1990), Negative pressure-temperature slopes for reactions forming $MgSiO_3$ perovskite from calorimetry, *Science*, *249*, 1275.

Kennett, B., and E. Engdahl (1991), Travel times for global earthquake location and phase identification, *Geophys J. Int.*, *105*, 429–465.

Langston, C. (1979), Structure under Mount Rainier, Washington, inferred from teleseismic body waves, *J. Geophys. Res.*, *84*(B9), 4749–4762.

Lawrence, J., and P. Shearer (2006), A global study of transition zone thickness using receiver functions, *J. Geophys. Res.*, *111*, B06307, doi:10.1029/2005JB003973.

Li, X., and X. Yuan (2003), Receiver functions in northeast China: Implications for slab penetration into the lower mantle in northwest Pacific subduction zone, *Earth Planet. Sci. Lett.*, *216*, 679–691.

Li, X., R. Kind, X. Yuan, S. Sobolev, W. Hanka, D. Ramesh, Y. Gu, and A. Dziewonski (2003), Seismic observation of narrow plumes in the oceanic upper mantle, *Geophys. Res. Lett.*, *30*(6), 1334, doi:10.1029/2002GL015411.

Ligorrìa, J., and C. Ammon (1999), Iterative deconvolution and receiver-function estimation, *Bull. Seismol. Soc. Am.*, *89*(5), 1395–1400.

Liu, K., S. Gao, P. Silver, and Y. Zhang (2003), Mantle layering across central South America, *J. Geophys. Res.*, *108*(B11), 2510, doi:10.1029/2002JB002208.

Qi, C., D. Zhao, Y. Chen, and N.A. Ruppert (2006), Tomographic imaging of the deep structure of the Alaska subduction, *Eos Trans. AGU*, *80*(46), West. Pac. Geophys. Meet. Suppl., Abstract T11A-0174.

Replumaz, A., H. Karason, R. van der Hilst, J. Besse, and P. Tapponnier (2004), 4-D evolution of SE Asia's mantle from geological reconstructions and seismic tomography, *Earth Planet. Sci. Lett.*, *221*, 103–115.

Ritsema, J., H. van Heijst, and J. Woodhouse (1999), Complex shear wave velocity structure imaged beneath Africa and Iceland, *Science*, *286*, 1925–1928.

Shearer, P. (1991), Constraints on upper mantle discontinuities from observations of long-period reflected and converted phases, *J. Geophys. Res.*, *96*(B11), 18,147–18,182.

Suito, K. (1977), Phase relations of pure Mg_2SiO_4 up to 200 kilobars, in *High Pressure Research. Academic*, edited by N. Manghani and S. Akimoto, pp. 255–266, New York.

Thirot, J., J. Montagner, and L. Vinnik (1998), Upper-mantle seismic discontinuities in a subduction zone (Japan) investigated from P to S converted waves, *Phys. Earth Planet. Inter.*, *108*, 61–80.

van der Meijde, M., S. van der Lee, and D. Giardini (2005), Seismic discontinuities in the Mediterranean mantle, *Phys. Earth Planet. Inter.*, *148*, 233–250.

Vinnik, L. (1977), Detection of waves converted from P to SV in the mantle, *Phys. Earth Planet. Inter.*, *15*, 39–45.

Wittlinger, G., and V. Farra (2007), Converted waves reveal a thick and layered tectosphere beneath the Kalahari super-craton, *Earth Planet. Sci. Lett.*, *254*, 404–415.

───────────────
E. Debayle, B. Tauzin, and G. Wittlinger, Ecole et Observatoire des Sciences de la Terre, CNRS and ULP, 5 rue René Descartes, 67084 Strasbourg Cedex, France. (benoit.tauzin@eost.u-strasbg.fr)